



Contents lists available at ScienceDirect

Acta Biomaterialia

journal homepage: www.elsevier.com/locate/actabiomat

Full length article

Embedding magnesium metallic particles in polycaprolactone nanofiber mesh improves applicability for biomedical applications [☆]

Udhab Adhikari ^{a,i,1}, Xiaoxian An ^{b,i,1}, Nava Rijal ^{c,i}, Tracy Hopkins ^{d,i}, Shalil Khanal ^{e,i}, Tom Chavez ^f, Rigwed Tatu ^d, Jagannathan Sankar ^{a,i}, Kevin J. Little ^g, David B. Hom ^h, Narayan Bhattarai ^{c,i,*}, Sarah K. Pixley ^{d,i,*}

^a Department of Mechanical Engineering, North Carolina A&T State University, Greensboro, NC 27411, USA

^b Department of Pharmaceutical Sciences, James L. Winkle College of Pharmacy, University of Cincinnati, Cincinnati, OH 45229, USA

^c Department of Chemical, Biological and Bioengineering, North Carolina A&T State University, Greensboro, NC 27411, USA

^d Department of Pharmacology and Systems Physiology, College of Medicine, University of Cincinnati, Cincinnati, OH 45267, USA

^e Department of Applied Science and Technology, North Carolina A&T State University, Greensboro, NC 27411, USA

^f College of Medicine, University of Cincinnati, Cincinnati, OH 45267, USA

^g Department of Orthopaedic Surgery, College of Medicine, University of Cincinnati, and Cincinnati Children's Hospital Medical Center, Cincinnati, OH 45267, USA

^h Head & Neck Surgery, Facial Plastic & Reconstructive Surgery, UC San Diego Medical Center, San Diego, CA 92103, USA

ⁱ NSF-ERC for Revolutionizing Metallic Biomaterials, North Carolina A&T State University, Greensboro, NC 27411, USA

ARTICLE INFO

Article history:

Received 10 December 2018

Received in revised form 28 April 2019

Accepted 30 April 2019

Available online xxx

Keywords:

Nanofiber

Polycaprolactone

Magnesium metal

In vitro metal degradation

In vivo metal implantation

Tissue engineering

Biomedical applications

ABSTRACT

Magnesium (Mg) metal is of great interest in biomedical applications, especially in tissue engineering. Mg exhibits excellent in vivo biocompatibility, biodegradability and, during degradation, releases Mg ions (Mg²⁺) with the potential to improve tissue repair. We used electrospinning technology to incorporate Mg particles into nanofibers. Various ratios of Mg metal microparticles (<44 μm diameter) were incorporated into nanofiber polycaprolactone (PCL) meshes. Physicochemical properties of the meshes were analyzed by scanning electron microscopy (SEM), Fourier-transform infrared spectroscopy (FTIR), mechanical tensile testing, X-ray diffractometry and UV–VIS spectrophotometry. Biological properties of meshes were evaluated in vitro and in vivo. Under mammalian cell culture conditions, Mg-containing meshes released hydrogen gas and relative amounts of free Mg²⁺ that reflected the Mg/PCL ratios. All meshes were non-cytotoxic for 3T3 fibroblasts and PC-12 pheochromocytoma cells. In vivo implantation under the skin of mice for 3, 8 and 28 days showed that Mg-containing meshes were well vascularized, with improved measures of inflammation and healing compared to meshes without Mg. Evidence included an earlier appearance and infiltration of tissue repairing macrophages and, after 28 days, evidence of more mature tissue remodeling. Thus, these new composite nanofiber meshes have promising material properties that mitigated inflammatory tissue responses to PCL alone and improved tissue healing, thus providing a suitable matrix for use in clinically relevant tissue engineering applications.

Statement of Significance

The biodegradable metal, magnesium, safely biodegrades in the body, releasing beneficial byproducts. To improve tissue delivery, magnesium metal particles were incorporated into electrospun nanofiber meshes composed of a biodegradable, biocompatible polymer, polycaprolactone (PCL). Magnesium addition, at several concentrations, did not alter PCL chemistry, but did alter physical properties. Under cell culture conditions, meshes released magnesium ions and hydrogen gas and were not cytotoxic for two cell types. After implantation in mice, the mesh with magnesium resulted in earlier appearance of M2-like, reparative macrophages and improved tissue healing versus mesh alone. This is in agreement with

[☆] Part of the Special Issue associated with the 10th International Conference on Biodegradable Metals, 10th Biometal 2018, held at the University of Oxford, 26–31 Aug. 2018, organized by Professors Diego Mantovani and Frank Witte.

* Corresponding authors at: Department of Chemical, Biological and Bioengineering, North Carolina A&T State University, Greensboro, NC 27411, USA (N. Bhattarai). Department of Pharmacology and Systems Physiology, University of Cincinnati College of Medicine, 231 Albert Sabin Way, MSB 4206A, Cincinnati, OH 45267-0765, USA (S.K. Pixley).

E-mail addresses: nbhattar@ncat.edu (N. Bhattarai), sarah.pixey@uc.edu (S.K. Pixley).

¹ Both contributed equally.

other studies showing beneficial effects of magnesium metal and provides a new type of scaffold material that will be useful in clinically relevant tissue engineering applications.

Published by Elsevier Ltd on behalf of Acta Materialia Inc.

1. Introduction

Nanofibers of various composition have received significant attention over the last two decades because they can be synthesized in various shapes, sizes and architectures to make tissue engineering scaffolds that can fill anatomical defects and provide the structural and biological support necessary for cell growth, proliferation, differentiation and motility [1–3]. Biocompatible and biologically useful nanofibers are produced by electrospinning, an established technique that produces small diameter fibers in the range of several nanometers to micrometers. Of particular interest is that electrospun nanofibers can mimic some properties of the extracellular matrix (ECM) and provide a 3D structure that enhances cell-material and cell-cell interactions [4]. Because of the wide choice of materials used to create nanofibers, and the readily available methods to control attachment of molecules and cells, electrospun nanofiber scaffolds have been used as a carrier matrix for controlled release of a wide range of materials including antibiotics, growth factors and other types of proteins, plasmid DNA and viable cells [5–9]. The advantages of using electrospun nanofibers in these applications include: high loading and encapsulation efficiency, polymer diversity to accommodate compatibility with physico-chemically distinct agents, ability to modulate release and process simplicity and cost-effectiveness [10–13].

Metals, in nano or micro particle form, have been added to electrospun nanofiber scaffolds without interfering with the biocompatibility, tunability and ability to mimic the ECM that make such scaffolds unique and biologically active [14]. Metals embedded into electrospun polymer nanofibers can improve the mechanical strength of the resulting scaffolds, as has been seen using nanoparticles of silver, gold, iron oxide, titanium, titanium oxide and magnesium oxide [15–18]. In addition to improving strength, metals can add important functions, such as making the scaffolds act as sensors, be antibacterial or catalytic, or absorb gases or toxins [15,16,19].

The biodegradable metal, Mg, has properties that have made it increasingly attractive to researchers interested in injury repair [20,21]. Because it is stronger and lighter than other metals, with bone-like tensile properties, the most extensively explored uses are as a solid metal implant providing physical support in orthopedic applications and as vascular stents. Orthopedic implants and stents containing Mg have been safely used clinically over the past several years in Europe and China [21], although implants are not yet approved for clinical use in the US. Mg implants have other important properties for tissue engineering because *in vivo* degradation produces two biologically active and potentially beneficial substances, hydrogen gas (H₂) and the Mg ion (Mg²⁺). Mg²⁺ is the second most abundant intracellular cation after K⁺ and the fourth most abundant in the body. Mg²⁺ is a crucial co-factor for over 300 enzymes [22]. Key reactions include the activation of ATPases, endonucleases, exonucleases, polymerases and phosphatases [23]. In orthopedic applications, Mg²⁺ stimulates new bone formation [24,25]. Increasing systemic levels of Mg²⁺, usually by injecting salt solutions, has been shown to be therapeutic for the respiratory and gastrointestinal systems, has reduced acute and chronic pain and has helped insomnia patients. Mg²⁺ salts have also been used in treatment of cardiac arrhythmias [23,26,27].

Of particular interest to us are the anti-inflammatory and neuroprotective roles of Mg²⁺. Anti-inflammatory effects were first

noticed because decreased blood levels of Mg²⁺ in humans and animals lead to significant systemic inflammation [28–30]. Further study has shown that Mg²⁺ influences lymphocyte development, reduces release of inflammatory cytokines and acts as a virtual immune system second messenger [28–30]. High Mg²⁺ levels also stimulate production of vascular endothelial growth factor (VEGF) in some cell types, which increases blood vessel growth during tissue healing [24].

Part of the neuroprotective effects of Mg²⁺ stem from the way the ion blocks calcium ion channels and a major glutamate receptor in brain tissues. Both actions reduce secondary damage of neurons after physical injury. Preclinical studies have shown that systemic or intraventricular application of Mg salts provided significant neuroprotection and improved functional recovery after strokes or brain damage [31]. Improving Mg²⁺ balance in the blood with the Mg salt, Mg threonate (which enhanced cerebrospinal fluid (CSF) levels after oral intake in rodents more effectively than other Mg salts [32]), has shown benefits in both preclinical and clinical studies of Alzheimer's disease [33,34].

The other beneficial product of degradation of Mg metal in aqueous solutions is hydrogen gas (H₂). Hydrogenated water (frequently produced for studies by Mg metal degradation in water) has been shown to be a strong antioxidant [35], with protective effects in several preclinical disease models, including those modeling Parkinson's disease and Alzheimer's, and clinical trials have shown effectiveness against cognitive decline [35–38]. However, these beneficial effects can only be realized if the production of hydrogen gas by *in vivo* implants is relatively slow, because a rapid rate of Mg degradation can create gas-filled cavities [39] that can put pressure on and damage adjacent tissues.

Previous work from our labs has shown that Mg metal microfilaments improved peripheral nerve regeneration across an injury gap when used inside hollow nerve guides [40,41]. The metal was well tolerated and its presence improved axonal outgrowth and reduced tissue inflammation over controls including another metal control (Ti), which suggests that Mg metal degradation products were important. While these are promising results, to further maximize potential neuroprotective benefits of Mg²⁺ release, we proposed that small metal particles, if embedded in the nerve guide material, would provide a faster local release of degradation products than Mg filaments (which took longer than 6 weeks to degrade) [40,41]. Furthermore, distributing Mg metal particles throughout the nanofiber scaffold, by embedding particles into the nanofibers during electrospinning, would allow control over the timing, consistency and placement of local delivery of Mg²⁺. Controlled delivery would be of significant use, not only in nerve repair, but also in many other tissue engineering applications.

PCL is a hydrophobic, semi-crystalline polymer that is FDA-approved and used in many biomedical applications due to its biocompatibility and biodegradability [42–44]. It has suitable viscoelastic properties for use in large-scale production of scaffolds of various sizes and architectures. Another advantage of using PCL as a component of hybrid nanofibers is that it is soluble in a wide range of organic solvents, like TFE (trifluoroethanol), DCM (dichloromethane), HFIP (hexafluoroisopropanol) and chloroform. Further, its miscibility with other unspinnable polymers can create solutions with a viscosity suitable for electrospinning.

While reports have described deposition of electrospun materials on the surface of Mg metal [45–47] and very interesting

anti-inflammatory properties have been reported after depositing Mg on or within a solid metal or polymeric material [48,49], there has not been, to our knowledge, research on incorporating metallic Mg into electrospun nanofibers, polycaprolactone (PCL) in particular.

We synthesized electrospun nanofiber meshes of Mg metal particles embedded in PCL nanofibers. We evaluated the impact of Mg addition on the physical, chemical, and mechanical properties of the meshes and then studied cellular and tissue responses using both in vitro and in vivo models. We hypothesized that Mg-containing nanofiber meshes would have more useful biological properties than control meshes containing PCL nanofibers alone. These properties will lead to future exploration of translational biomedical applications.

2. Materials and methods

2.1. Materials

PCL (Mn 70–90 kDa), Mg particle powder (mesh size 325), and fetal bovine serum (FBS) were purchased from Sigma Aldrich (Saint Louis, MO, now Millipore Sigma). 2,2,2-Trifluoroethanol (TFE) was obtained from Alfa Aesar (Ward Hill, MA). The Xylidyl blue assay was either based on or done with kits from Stanbio Laboratory, Boerne, TX, USA). The Alamar Blue assay materials or kit, Dulbecco's phosphate-buffered saline (PBS), and Dulbecco's modified Eagle's medium (DMEM) were obtained from Life Technologies (Grand Island, NY, USA). Materials not otherwise specified were from Thermo Fisher Scientific (Waltham, MA or Florence, KY).

2.2. Mg/PCL solution preparation

The commercially prepared Mg metal powder, mesh size 325, has particles <44 μm . Suspensions of these Mg particles in liquid PCL (Mg/PCL solutions) were created by first dispersing Mg metal powder in anhydrous TFE under an argon atmosphere and then adding dry PCL pellets. Proportions were adjusted to give different w/w proportions of the two dry ingredients (Table 1). The weight of PCL was kept at 10% of the weight of TFE. To create uniform suspensions prior to spinning, the mixtures were subjected to constant magnetic stirring for 24 h at room temperature.

2.3. Electrospinning Mg/PCL nanofibers

Electrospun nanofiber meshes of PCL and Mg/PCL were prepared as described in our previous publications [50,51]. In brief, the electrospinning apparatus consisted of a syringe pump (Model 78-01001, Fisher Scientific, Pittsburgh, PA, USA), a high-voltage power supply (Model CZE100PN30, Spellman High Voltage Electronics Corporation, Hauppauge, NY, USA) and a BD Luer-Lok syringe with an attached 18G-diameter hypodermic needle. The needle-to-collector distance was maintained at 7 cm, with an applied voltage of 20 kV. The feeding rate of the solution was precisely controlled by a syringe pump system, which was adjusted to a flow rate of 2.5 ml/h. The fibers deposited onto an aluminum foil-wrapped rotating grounded collector were left overnight in dust-free conditions at room temperature, to allow complete solvent evaporation. The nanofiber meshes were removed from the collector and detached from the aluminum foil for physical, chemical and biological characterization.

2.4. Dynamic light scattering (DLS) analysis

A Zetasizer Nano ZS (Malvern Instruments, Malvern, UK) was used to measure the hydrodynamic size distribution of the Mg par-

Table 1

Mesh designations, mesh composition (proportions of dry materials added) and final percentage of Mg metal (w:w%) in the electrospun material deposited on the collecting drum after drying.

Nanofiber Mesh	Proportions of dry Mg:PCL (w:w)	Mg (w:w%) in dried mesh
PM-0	0:100	0
PM-10	10:100	9
PM-20	20:100	16
PM-30	30:100	23
PM-50	50:100	33

ticles. Mg metal powder (0.1 g of as-received material) was dispersed in 10 ml of anhydrous ethanol and a 1 ml sample was loaded in a cuvette for DLS analysis. Intensity measurements, indicating the total percent of beam scattering by size category, were converted into terms of volume and number averages using Mie Theory.

2.5. Surface morphology analysis

The surface morphologies of Mg particles alone and Mg-containing meshes were analyzed using a scanning electron microscope (SEM, Hitachi SU8000, Tokyo, Japan) and a transmission electron microscope (TEM, Tecnai G2 Twin, Hillsboro, OR). A single drop of the Mg suspension in ethanol (see preparation for DLS above) was deposited on double-sided conductive copper tape (for SEM) or a carbon grid (for TEM) and dried under ambient conditions for 20 min before being observed under the respective electron microscope. Mesh samples were cut and deposited on copper tape and sputter-coated with gold using a Polaron SEM coating system (Quorum Technologies, East Sussex, UK) for 90 s at 15 mA. SEM images were taken at an accelerating voltage of 10 kV and 5 μA current. Image-Pro Plus 6.0 software (Media Cybernetics, Inc., Rockville, MD) was used to measure nanofiber diameters in SEM images.

The apparent density and porosity of nanofiber meshes were estimated using the following equations [52]:

$$\text{apparent density} = \frac{\text{mass of mesh}}{\text{mesh thickness} \times \text{mesh area}} \quad (1)$$

$$\text{porosity} = 1 - \frac{\text{apparent density}}{\text{PCL or PCL/Mg bulk density}} \quad (2)$$

$$\text{bulk density} = \frac{1}{\left(\frac{w_1}{d_1} + \frac{w_2}{d_2}\right)} \quad (3)$$

where w_1 & w_2 are weight fractions and d_1 & d_2 are densities of PCL and Mg, respectively. Thickness of mesh samples was measured using a digital micrometer.

2.6. X-ray diffraction analysis

A Bruker AXS D8 Discover X-ray diffractometer (Billerica, MA) with Cu-K α radiation was used to examine diffraction patterns of the meshes. X-ray diffraction (XRD) was performed using a locked-coupled scan with a scanning range (diffraction angle, 2θ) set between 10° and 60° , in continuous mode, in increments of 0.0146° , 2θ , at room temperature.

2.7. FTIR analysis

Fourier-transform infrared spectroscopy (FTIR) was used to identify functional groups and chemical interactions between PCL and Mg in the meshes. FTIR spectra were obtained with a Varian

670 FT-IR Spectrophotometer (Varian, Inc., Palo Alto, CA, USA) in the range of 4000 to 600 cm^{-1} region. Selected IR bands of carbonyl and esters groups, and CH bending were analyzed to illustrate the changes that the PCL polymer underwent during electrospinning with Mg particles.

2.8. Mechanical properties

Mechanical properties of the meshes were determined using an Instron 5542 (Canton, MA, USA) with a 500 N load cell at a displacement rate of 4 mm/min. A custom designed specimen holder was used to test the strength of the meshes. To avoid any damage during handling and to maintain uniformity in loading conditions, a custom designed paper template (40 × 10 mm) was used as a specimen holder. The template consisted of two halves, top and bottom, and held the sample sandwiched between them with the aid of double-sided adhesive tape. A five mm length at both ends was allowed for pneumatic jaw gripping, leaving 30 mm as the gauge length. The two halves of the template were cut off prior to the start of the test. Samples were strained to breakage, stress-strain curves were created, and the data were used to calculate Young's modulus (YM), ultimate tensile strength (UTS) and breaking strain.

2.9. In vitro release of Mg^{2+} and hydrogen

To determine free Mg^{2+} release in vitro, mesh pieces (1 × 1 cm) were attached to 24-well plates (n = 4 per mesh), using a biocompatible silicone-based elastomeric glue (Kwik-Sil™, Sarasota, FL, USA). In a sterile culture hood, samples were sterilized by immersion in 95% ethanol (20 mins), air drying and exposure to UV light (20 mins per side). Mesh pieces were briefly washed with sterile water and 1 ml of cell culture medium was added (DMEM + = DMEM supplemented with 10% fetal bovine serum (FBS) and 1% antibiotics (10,000 units/ml of penicillin and 10,000 $\mu\text{g}/\text{ml}$ of streptomycin)). Wells were capped and maintained in a cell culture incubator (humid, 5% CO_2 , 37 °C). At each time interval, the medium was removed and replenished (1 ml DMEM+). Cumulative free Mg^{2+} concentration in the collected medium was determined using a colorimetric Xylidyl blue assay, which is widely used in determining free Mg^{2+} level in human blood, serum and urine [53]. The Xylidyl blue dye reagent, at alkaline pH, combines with Mg^{2+} to form a purple complex whose color, measured by spectrophotometry, is proportional to Mg^{2+} concentrations. Standard curves of MgSO_4 in medium were used to convert to mmoles of Mg and the values for basal medium (contains ~0.8 mM Mg) were subtracted to give release due only to the Mg in the mesh. Use of basal medium as a control also avoided interference by sodium phosphate in culture medium, which could possibly form insoluble Mg salts and add variability. The dye reagent was added to samples and standards at the concentration recommended by the manufacturer, incubated for 1 h at room temperature and absorbance was measured using a SpectraMax M2 Spectrophotometer (Molecular Devices, San Jose, CA, USA) at 520 nm.

Table 2

Cell culture information and experimental parameters used to analyze electrospun mesh cytocompatibility in vitro.

Cell line	Test	Assay Type	Substrate	Media	Plating density ($\#/\text{cm}^2$)	Time (days)	Assay
3T3	Viability	Direct*	Mesh, Control = PM-0	DMEM	63,700	1,2,3	Alamar Blue
	Attachment	Direct*	Mesh	DMEM	63,700	3	SEM
PC-12	Viability	Indirect**	Plastic + poly-L-lysine	Mesh extracts	50,000	1	Alamar Blue
	Attachment	Direct*	Mesh + poly-L-lysine	RPMI	50,000	7	SEM

* Direct assay: cells were plated directly on the mesh.

** Indirect assay: cells were plated on the indicated substrate.

To determine H_2 release, mesh pieces (1 × 1 cm, n = 3 per mesh type) were attached to the bottom of a T25 flask (1 piece/flask) with Kwik-Sil™ and DMEM (5 ml, no serum or antibiotics) was added, the flask was capped tightly (non gas-permeable caps) and incubated at 37 °C for 24 h. An amperometric H_2 microsensor connected to a multimeter (both from Unisense A/S, Aarhus N, Denmark) was allowed to stabilize in deionized water and calibrated (H_2 concentration versus current (pA)) using decreasing dilutions of H_2 saturated deionized water). To measure the H_2 produced by the mesh, the flasks were opened, the sensor tip was immersed and measurements were taken for 3 min. Calibration was repeated after measuring all flasks. When converting current to H_2 concentration, the values during the first 30 s (which included sensor movement artifacts) and the last 30 secs (where a decline occurred due to loss of H_2) were excluded and the remaining values were averaged.

2.10. Mesh thickness in vitro

To analyze mesh thickness when dry and after three days of incubation in a cell culture medium (DMEM+, in an incubator), mesh pieces (dry or wet) were placed on slides, coverslipped and viewed by confocal microscopy (Zeiss LSM510 META microscope, Carl Zeiss AG, Oberkochen, Germany) under a 40X objective. Z-stack 3D pictures were taken and the thickness of XY transections were thresholded and measured using NIH ImageJ software.

2.11. Cell viability and attachment to mesh

NIH-3T3 cells (a mouse fibroblast cell line, ATCC 1658) and PC-12 cells (a cell line derived from a pheochromocytoma of the rat adrenal medulla, ATCC CRL-1721) (ATCC, Manassas, VA) were maintained in their respective media (DMEM+ or RPMI with serum and antibiotics, as recommended by ATCC), in 5% CO_2 in a cell culture incubator. Media and conditions of culture and assays are outlined in Table 2. Substrate preparation was different between cell lines. For 3T3 studies, mesh pieces were placed over circular 10 mm diameter coverslips, attached underneath with Kwik-Sil™ and then placed in wells of a 24 well plate. For PC-12 studies, mesh pieces were attached to the culture plastic in 48 well plates with Kwik-Sil™. For both, mesh samples were sterilized (as described above). For 3T3 cells, mesh samples were preincubated in the medium for 3 h before cells were added. For PC-12 cells, substrates were precoated with poly-L-lysine (0.1 mg/ml, 1 h, removed and cells in media were added). Medium was replaced every 2 days, where appropriate. For the indirect assay (used for cell viability of PC-12 cells), mesh extracts were prepared by incubating mesh pieces (0.7 × 0.7 cm) in medium (490 μl RPMI medium, in 48 well plates) for 3 days in an incubator, then medium was removed and added to cells without dilution or delay. Cells were then analyzed after a one-day exposure to extracts. In all cases, at least three pieces of each mesh type were used per set of cells and data shown are either averages of multiple experiments or from one experiment that was representative of multiple experiments with similar results.

Cell viability for 3T3 and PC-12 cells was monitored with an Alamar Blue (AB) colorimetric assay. The dye, AB, contains the chemical, resazurin, which enters living cells where mitochondrial reductases reduce the blue and non-fluorescent resazurin to resorufin, which emits pink fluorescence [54]. The amount of dye reduced (the amount of fluorescence) is proportional to cellular metabolic activity, which is proportional to cell number. For this assay, medium was removed from the cells, cells were washed twice with PBS and then incubated for two hours with 10% (v/v) AB reagent in the respective culture medium. Assay solutions were transferred to fresh plates and multiple aliquots were taken to measure fluorescence on a spectrophotometer (as above) or on a plate reader (SpectraMax M2 Spectrophotometer, Molecular Devices, San Jose, CA, USA) with excitation at 530 nm and emission at 590 nm. Cell viability was calculated using the following equation:

$$\text{Cell viability} = \frac{(\text{fluorescence of the samples} - \text{fluorescence of the blank})}{(\text{fluorescence of the control} - \text{fluorescence of the blank})} \times 100\%$$

Cells were prepared for SEM by rinsing with PBS (two brief rinses) and fixation with 4% glutaraldehyde (30 min). After fixation, cells were briefly rinsed with deionized water (2 times) and dehydrated (sequential incubations in 50, 75 and 100% ethanol, 10 min each) at room temperature. The samples were left to dry in a sterile fume hood for 24 h before coating with metal and imaging (as for mesh, above).

2.12. In vivo implantation and tissue processing

2.12.1. Animals

A total of 42 female C57/Bl6 mice, age 21–28 days, were purchased from Jackson Labs and housed in micro-isolator cages in AAALAC approved animal facilities. All care, handling and procedures were approved by the University of Cincinnati Institutional Animal Care and Use Committee and were in accordance with the NIH Guide for the Care and Use of Laboratory Animals. The experimental groups were PM-0 (5 mice/group), PM-10 (5 mice/group) and sham operated (4 mice/group) animals, at three time periods: 3, 8 and 28 days survival.

2.12.2. Surgery

Animals were anesthetized with isoflurane, the dorsal mid-body area was shaved and an area approximately 6 × 6 cm was cleaned three times with alternating betadine and alcohol. A small incision was made under the skin on the back above the hip on each side of the animal and a pocket was created by inserting forceps toward the tail. Mesh pieces, 1 × 1 cm, were sterilized (as above) and one piece of dry mesh was inserted into each pocket, while preventing doubling. Wounds were stapled shut and animals were allowed to recover. Meloxicam (Eloxiject, Henry Schein, 5 mg/ml) was given at 5 mg/kg, once daily for 3 days for pain prevention.

2.12.3. Tissue preparation

On days 3, 8 and 28 after surgery, mice were euthanized by approved methods, the skin with attached mesh was removed, fixed (4% paraformaldehyde in 0.1 M PBS, 24 h, room temperature), rinsed and paraffin embedded (standard procedures). Sections were cut (8 μm) onto Superfrost slides.

2.12.4. Staining and immunostaining

Slides were dewaxed, rehydrated in decreasing concentrations of ethanol to water, then stained with hematoxylin & eosin

(H&E), Masson's trichrome (kit from Newcomer's Supply, Middleton, WI) or immunostained. For immunostaining, using techniques described previously [40,55], M2-like macrophages (non-classically activated, tissue reparative) were identified with a rabbit polyclonal antibody to liver arginase-1 (Arg1, 1:500, Abcam, Cambridge, MA) and secondary Alexa Fluor 594 goat anti-rabbit (1:1000). M1-type macrophages (classically activated, pro-inflammatory) were identified with a mouse monoclonal antibody to inducible nitric oxide synthase (iNOS, 1:500, Santa Cruz Biotech, Dallas, TX) and secondary Alexa Fluor 488 goat anti-mouse (1:1000). As the anti-iNOS staining signal to noise difference was adequate for quantification, no adjustment was used for mouse antibodies used on mouse sections. Immunostaining for nerve fibers expressing CGRP was done by combining an axon-specific rabbit antibody against the heavy molecular weight (MW 200) neurofilament protein (NF, 1:500, Sigma Aldrich, St. Louis, MO) and secondary Alexa Fluor 594 donkey-anti-rabbit (1:1000) to label axons and goat anti-CGRP (1:1000) with secondary donkey Alexa Fluor 488 anti-goat (1:1000). All slides were stained for nuclei with 4',6-diamidino-2-phenylindole dihydrochloride (DAPI, 1:1000, blue in images) diluted into the mounting medium, Fluoromount. All antibodies and materials not otherwise indicated throughout the methods were from Thermo Fisher Scientific (Florence, KY).

2.12.5. Microscopy, photography and image analysis

Color images were taken with a Zeiss Axiocam digital camera on a Zeiss Axioplan imaging 2e fluorescence microscope. Fluorescence images were photographed with a QICam, cooled, black and white CCD camera (QImaging, Canada), with excellent resolution at low light levels. Photographs of monochrome images used for quantification were taken with consistent lighting and exposure times. Composites, pseudocoloring of fluorescent images and figure arrangements were done with Photoshop (Adobe Systems Inc.). Analysis of photomicrographs was performed with ImageJ software (NIH), by viewers blinded to conditions. In all cases, images were taken from multiple sections per animal and multiple measurements were made and averaged per image. Averages of all section data per animal were used for statistical analysis. In some cases, meshes were not recovered from an animal at a certain time point, or there were technical difficulties, resulting in an n of 4 instead of 5.

2.13. Statistics

SPSS Statistics 17.0 software or SigmaPlot (v13, SysStat Software, Inc., San Jose, CA) were used to conduct statistical analyses, with significance assumed at $p < 0.05$. Observers were blinded to conditions. As most n values were between 3 and 5, non-parametric statistics were used for most analyses, with a Mann-Whitney Rank sum test for two variables or, for >2 variables, a Kruskal-Wallis ANOVA on Ranks, with Dunn's post-hoc tests when groups had unequal numbers or Student-Newman-Keuls post-hoc tests if equal numbers. Box plots were used to show median, 25/75 percentiles and 5/95% error bars and averages per animal were added as triangles overlaid on the box plots. Parametric analyses were used for two-way ANOVA analysis of changes in vivo mesh parameters over time (Figs. 6, 7) and for analysis of cumulative release of Mg ions from mesh pieces immersed in cell culture medium (one-way ANOVA and Holm-Sidak post-hoc, Supplemental Fig. 2), to take into account the cumulative standard deviations (generated by summing variances). Bar graphs were used with parametric analyses. To compare slopes for data over time, a parallel lines analysis (a test for equality of slope) was used. For all in vivo analyses, data were averages per mouse.

3. Results

3.1. Mg particle characterization

The as-received Mg particles used to incorporate into the PCL nanofibers were smaller than 44 μm diameter and irregularly shaped, as shown by SEM imaging in Fig. 1A and TEM in Fig. 1B. Fig. 1C shows the X-ray diffraction data for the particles, with peaks that are consistent with the known crystallographic planes of magnesium [56]. The mean hydrodynamic diameter of most of the particles was distributed around 100 nm (Fig. 1D) and the volume percent was distributed around 1000 nm (Fig. 1E), which is in good agreement with the SEM and TEM images (Fig. 1A and B).

3.2. Nanofiber fabrication and characterization

Mg particles were dispersed in PCL/TFE and electrospun to create nanofiber meshes, as shown in Fig. 2. Based on SEM images (Figs. 2, 3 and Supplemental Fig. 1A–C) and TEM images (Supplemental Fig. 1E), two phenomena were occurring, as outlined in the schematics in Fig. 2: (a) Mg particles with diameters smaller than the fiber diameter were incorporated within individual PCL fibers and (b) Mg particles with diameters greater than fiber diameters were coated with PCL and attached via weak surface links to fibers and/or suspended within the mesh of multiple fibers.

Fig. 3 shows the changes in PCL fiber morphology with increasing Mg concentrations (Table 1 shows relative Mg/PCL proportions). The SEM images show randomly interconnected structures and a smooth morphology of most electrospun PCL nanofibers. Mg particles larger than the fiber diameters are clearly visible in SEM images of Mg-containing nanofibers. The presence of Mg particles within the meshes was confirmed by EDS mapping

(Supplemental Fig. 1) of different locations in PM-50. The relative percentages of elements (e.g. Mg, C and O) in the composite fiber mesh at selected positions are presented in Supplemental Table 1.

As seen in the distribution graph in Fig. 3, as the Mg content incorporated into meshes increased, the number of larger diameter fibers increased. Per type of mesh, 98% of fibers had diameters in the range of 200–2800 nm for PM-0 (average diameter 1.38 ± 0.58), 200–3000 nm for PM-10 (avg. 1.49 ± 0.62), 200–3400 nm for PM-30 (avg. 1.44 ± 0.68) and 200–4400 nm for PM-50 (avg. 1.61 ± 0.87). However, only PM-0 and PM-50 were significantly different (ANOVA, $p = 0.021$, $n = 150$). Note that only PM-30 and PM-50 had a subset of fibers larger than 3000 nm.

Porosity of the meshes was estimated after calculating the bulk density of the mesh, as described in Methods (Section 2.5). The porosity for PM-0, PM-10, PM-30 and PM-50 was (in %) 62 ± 6.3 , 61 ± 5.3 , 64 ± 3.3 and 69 ± 8.5 , respectively. None of the values were significantly different (ANOVA, $p > 0.05$, $n = 3$).

3.3. X-ray diffraction and FTIR analysis of electrospun meshes

Addition of Mg particles to the PCL polymer could alter the chemistry of the final Mg/PCL composites. To analyze whether this occurred, X-ray Diffraction (XRD) patterns and FTIR spectra were obtained for each mesh type.

The XRD patterns of as-spun Mg/PCL nanofibers are shown in Fig. 4A. The PM-0 mesh showed two strong peaks at 21.5° and 23.6° , corresponding to the (110) and (200) crystallographic planes of PCL [51]. In PCL nanofiber samples containing Mg, major peaks were observed at 32.2° , 34.4° , 36.6° , 47.8° and 57.4° , corresponding to the (100), (002), (101), (102), and (110) crystallographic planes of Mg, respectively [56]. The intensity of both the PCL peaks at

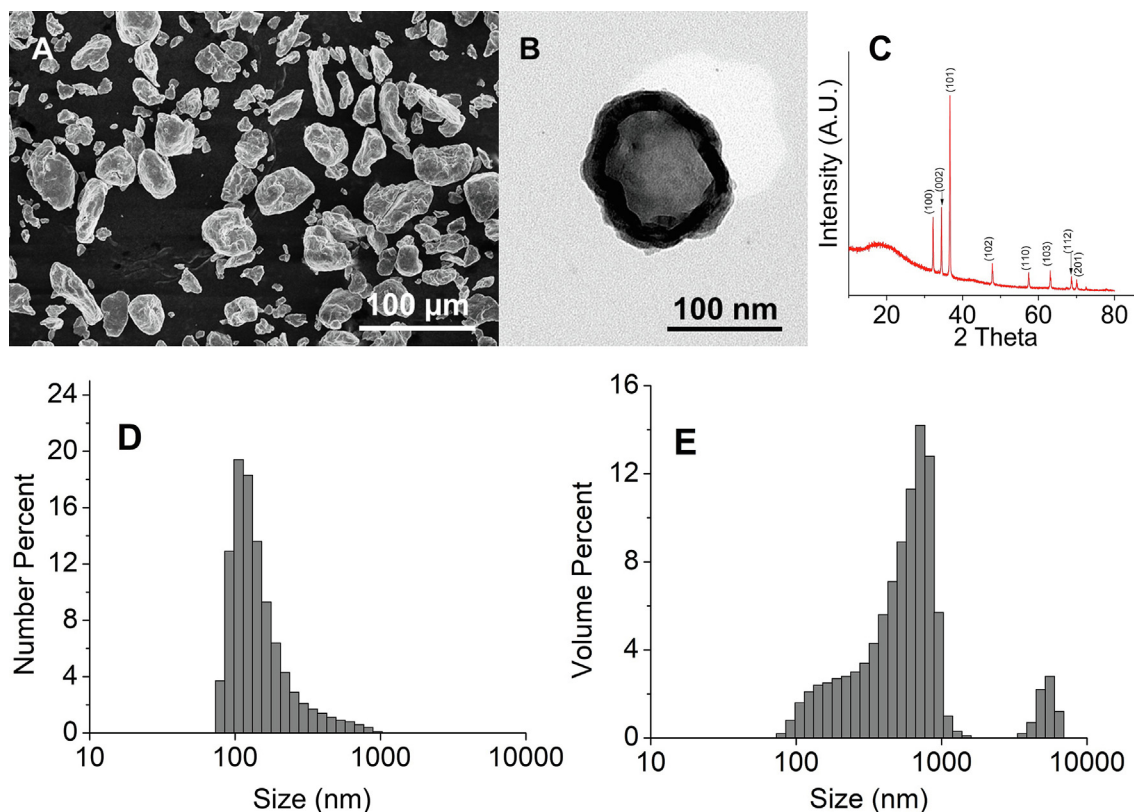


Fig. 1. Characterization of as-received Mg metal particle powder. (A) SEM image, (B) TEM image, (C) X-ray diffraction pattern showing crystallographic planes of magnesium. (D, E) The size distribution of Mg particles in the as-received powder was measured by a dynamic light scattering (DLS) technique. The mean hydrodynamic diameter of the particles was measured from number- and volume-weighted distributions obtained from DLS.

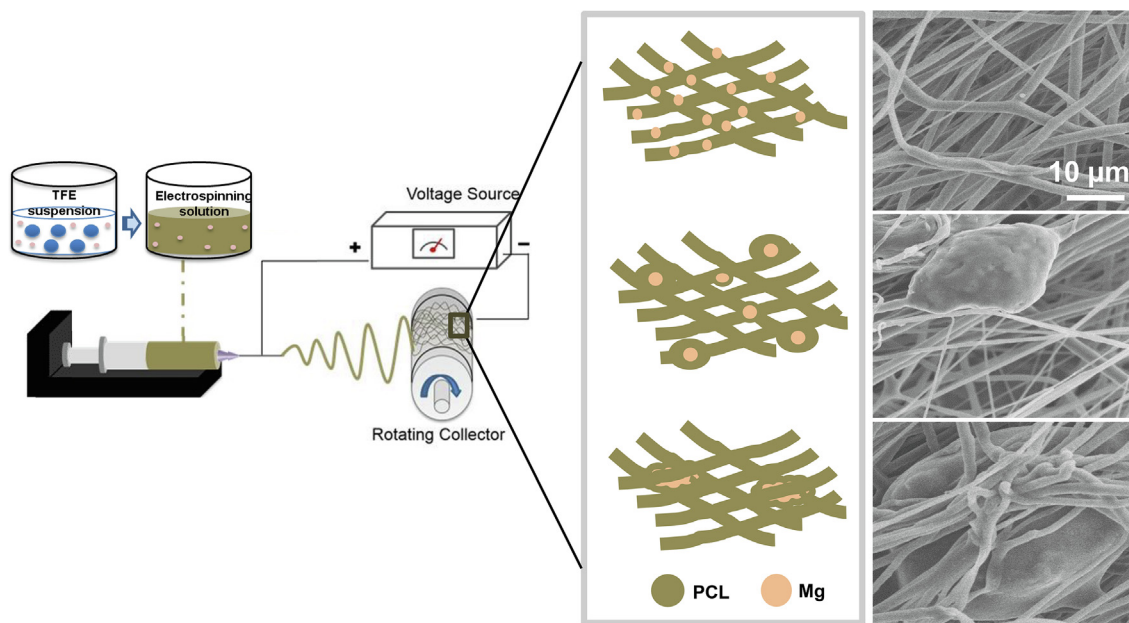


Fig. 2. Fabrication of PCL-Mg composite nanofiber mesh. This schematic illustration shows how suspensions of Mg/PCL in anhydrous TFE were electrospun using a custom-built electrospinning apparatus. Fibers were deposited onto a rotating, grounded collector and then detached for physical and biological characterization. Mg particles became enmeshed within the PCL nanofibers according to particle size and morphology, as depicted in the drawings (middle) and shown in the SEM images (right).

21.5° and 23.6° decreased for PM-30 and PM-50, revealing a decrease in degree of crystallinity of PCL. The intensity of the Mg peaks increased as the concentration was increased from PM-10 to PM-50. The appearance of the same crystallographic peaks of Mg in all fiber samples and the lack of significant peaks of Mg oxidation products strongly suggest that the Mg metallic particles are imbedded in the nanofiber meshes in ways that prevent their oxidation.

Possible chemical interactions between PCL and Mg within the as-spun nanofibers were examined by FTIR and the spectra are shown in Fig. 4B. Typical absorption bands for PM-0 were located at: 1726 cm^{-1} for stretching of C=O in esters; 1360, 1397 and 1473 cm^{-1} for bending of CH; 2942 and 2858 cm^{-1} for stretching of CH_2 ; 1160 and 1290 cm^{-1} for stretching of C–O and C–C in the amorphous and crystalline phases and 1042, 1107, and 1233 cm^{-1} for the stretching vibration of C–O–C [57]. All of the peaks found in PM-0 were also present in the Mg meshes. This suggests that addition of Mg did not significantly alter the chemical structure of PCL. Further evidence that addition of Mg does not cause structural changes in the PCL was provided by comparing the relative contributions of the C–O, C–O–C, C–C and C=O bands with respect to the –CH band at 1360 cm^{-1} . As seen in Fig. 4C, the relative absorbance for each comparison did not change with Mg content.

3.4. Mechanical testing

The addition of a particulate into a polymer via electrospinning is expected to significantly alter the mechanical properties, but predicting the exact nature of the changes is complicated, so they were confirmed here empirically [58–60] and summarized in Table 3. Mechanical properties of mesh types were assessed via tensile tests. Fig. 4D shows stress versus strain curves for one batch (B1) of PCL and Mg/PCL mesh. The Young's modulus was determined using Hooke's law from the slope of the linear portion of the stress-strain curve (Fig. 4E, Table 3). The ultimate tensile strength represents the highest stress that a nanofiber sample could bear without breaking (Fig. 4F, Table 3). For both measures,

the PM-0 and PM-10 values were not different and addition of further amounts of Mg resulted in incremental and significant decreases (Fig. 4E and F, Table 3). Breaking strains, the highest strain needed for breakage, a measure of material ductility and determined from the stress-strain curves, were significantly different between all groups, with PM-0 having the highest ductility, and brittleness increasing with higher amounts of Mg (Table 3).

3.5. *In vitro* Mg²⁺ release

To gain an understanding of the time course of Mg metal degradation, release of free Mg²⁺ was measured after pieces of each mesh were immersed in a standard cell culture medium and maintained in a cell culture incubator for 14 days (336 h). All meshes, from two mesh batches (B1 and B2), a total of eight conditions, were tested and four separate pieces of mesh were tested per condition and medium was completely replaced at several time points. Cumulative free Mg²⁺ release, analyzed using a Xylidyl blue dye assay, is shown in Fig. 5A. Notable was that the cumulative release for the PM-10 meshes, from each batch, showed a slowing of release over time, while all other meshes with higher amounts of Mg (PM > 10) maintained a steady, essentially linear, increase in release throughout. Analysis of the final cumulative release (Supplemental Fig. 2A), showed that most of the four mesh types with PM > 10 were similar, with only Batch 2, PM-20 (abbreviated PM-20(2)) different from PM-50(1). The four PM > 10 meshes were different from all of the other mesh types. By this analysis, total cumulative release for PM-10(1) was not different from either PM-0(1,2). However, release from PM-10(1) was significantly higher than PM-0(1) at each separate time point, so this result probably reflects the variability across the entire data set. To examine batch differences, cumulative release values were compared for PM-10(1,2) and PM-30(1,2) meshes. As shown in Supplemental Fig. 2B, cumulative release for PM-10, but not PM-30, differed between batches, suggesting no consistent difference in release across batches.

The cumulative release curves (Fig. 5A) suggested that the rates of Mg release might be the highest initially. To characterize rate

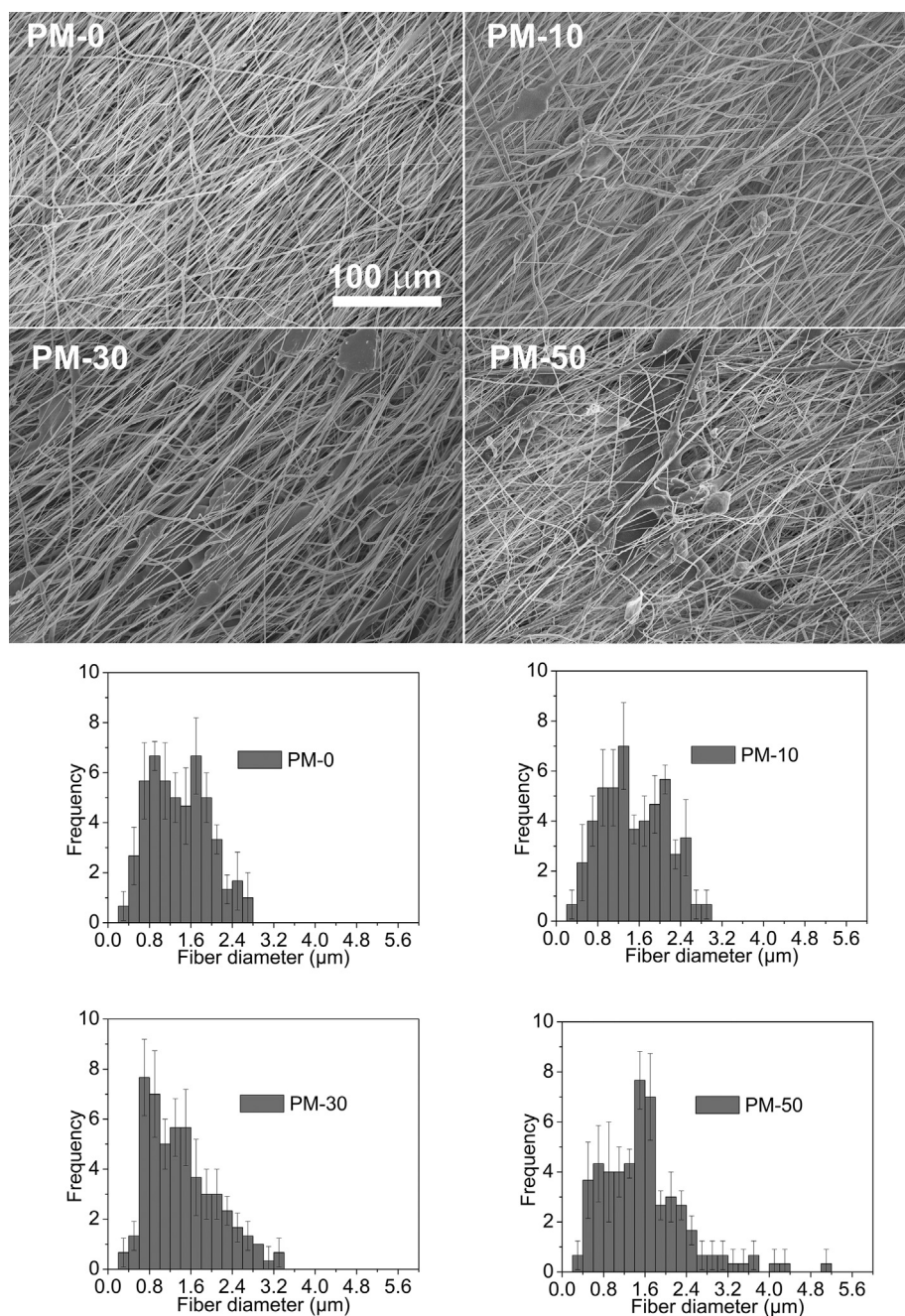


Fig. 3. Surface morphology and diameter distributions of electrospun nanofiber mesh, from Batch 1 meshes (PM-0, PM-10, PM-30 and PM-50). Top: SEM images of the nanofiber meshes. Bottom: Distribution of fiber diameters measured using Image-Pro Plus 6.0 software. Averages and standard deviations are given for analysis of fibers in three images ($n = 150$).

changes, rates of release were calculated for each medium change (Mg release at the end of the time period divided by hours between medium changes) (Supplemental Fig. 3). As shown in Supplemental Fig. 3A, the rates of release over the first 2 h (to the first medium change) were much higher than all subsequent rates. Release after 24 h was relatively constant, with some gradual decline with the PM-10 mesh. The 0–2 h rates were approximately 10 fold higher (maximum around 0.0006 mmoles/hr, Supplemental Fig. 3B) than over the last time period (240–336 h, maximum around 0.00006, Supplemental Fig. 3C). For the 0–2 h release rates, there were significant differences between many of the mesh types, while for the final time period, 240–336 h, there were fewer significant differ-

ences, with a trend that the lowest rates were for the PM-10 mesh. A very low final rate of release for PM-10 meshes was consistent with the reduction in particles seen in light microscopic (LM) images (Supplemental Fig. 4)

Overall, because our interest was to eventually use these meshes for nerve repair, we chose to further examine the in vivo effects of implanting a PM-10 mesh that produced an initial burst of Mg release and then reduced release at later time periods. This is because Mg ions are neuroprotective after nerve injury, but if levels are maintained above physiological for too long, there are negative effects on ionic balance and thus functions of neurons [61].

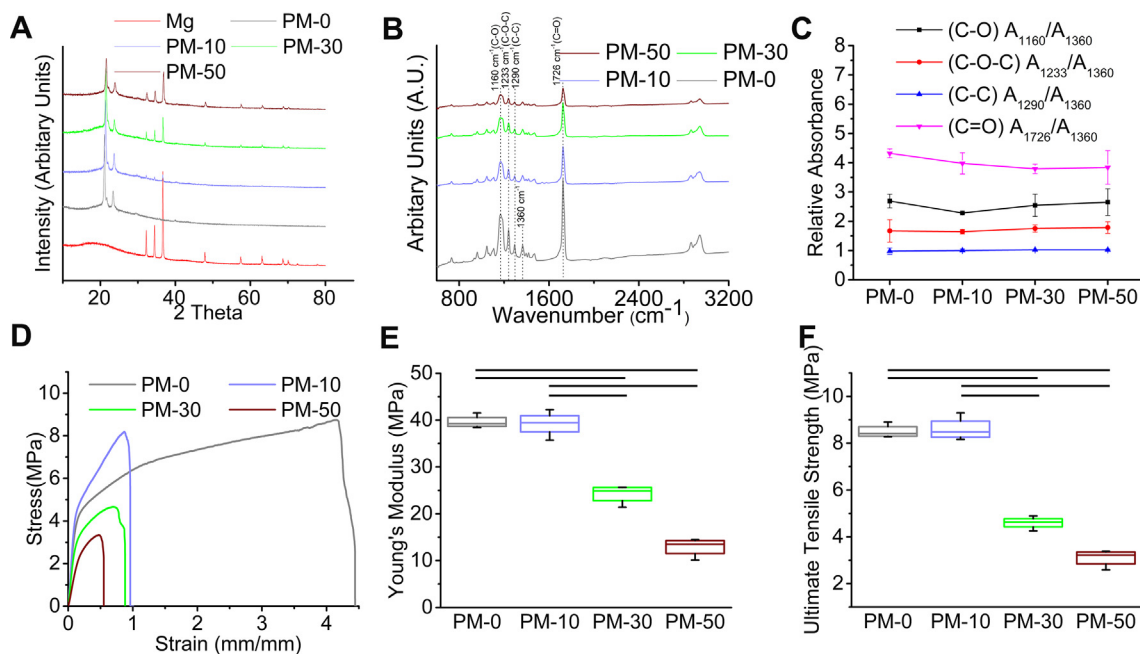


Fig. 4. Crystalline phases, chemical structure and mechanical properties of nanofiber meshes (Batch 1). (A) XRD patterns allow comparisons of crystalline planes and (B) FTIR spectra allow comparisons of chemical interactions between PCL and Mg among the mesh types. (C) Further analysis of the relative contributions of the C–O, C–O–C, C–C and C=O bands with respect to the –CH band at 1360 cm^{-1} is shown as a function of Mg content in the FTIR spectra of B. (D–F) Mechanical properties were examined by tensile testing. (D) A representative set of tensile stress-strain curves. (E) Averaged comparisons of Young's modulus and (F) averaged ultimate tensile strength at break. Bars indicate significant differences (ANOVA, $p = 0.005$ for each, $n = 3$).

Table 3
Mesh Mechanical Properties (Batch 1).

Nanofibrous Mesh	Young's Modulus (MPa)	Ultimate Tensile Strength (MPa)	Breaking Strain (mm/mm)
PM-0	39.6 ± 1.6	8.5 ± 0.3	4.1 ± 0.1
PM-10	39.2 ± 3.2	8.6 ± 0.6	0.96 ± 0.1
PM-30	24.2 ± 2.4	4.6 ± 0.3	0.80 ± 0.03
PM-50	12.9 ± 2.4	3.1 ± 0.4	0.50 ± 0.02

3.6. In vitro hydrogen release

Nanofiber meshes from Batch 2 were tested for release of H_2 after 24 h immersion in cell culture medium, using an amperometric hydrogen microsensor. All mesh types released significant amounts of H_2 compared to PM-0 mesh, but there were no differences between meshes with different Mg content (Fig. 5B).

3.7. In vitro cytotoxicity

Cytotoxicity was assessed in vitro using cell lines representing both fibroblasts (3T3 cells) and neuron-like cells (PC-12 cells) and an Alamar Blue assay. For 3T3 cells, cell viability was examined by plating the cells directly onto meshes, with time periods of 1, 2 and 3 days. As seen in Fig. 5C, although there was some decrease in viability for the higher Mg content meshes after 3 days (cell viabilities for PM-30 and PM-50 were 69 and 74% of the PM-0 control, respectively), none of the values were significantly different from controls. Per the current ISO standards (ISO-10993-5), cell viability higher than 75% is considered to indicate no toxicity, in evaluation for medical devices [62].

For PC-12 cells, an indirect cell viability test was chosen because PC-12 cells attach poorly to substrates or aggregate into clusters that can readily detach. While SEM images showed that PC-12 cells could attach to the meshes (Fig. 5F), this contributed to high assay variability so an indirect assay was chosen. ISO-

10993-5 conditions were used to prepare extracts of each mesh [62] and meshes were precoated with poly-L-lysine to increase PC-12 cell attachment [63]. As shown in Fig. 5D, viability of PC-12 cells (one-day assay) was above 75%, with no differences between conditions. Thus, all meshes were non-toxic. To ensure that the Mg^{2+} released was not within toxic levels, free ion levels were measured (Xylidyl blue assay) and the maximum level, for the PM-50 mesh, averaged around 5 mM (data not shown), which is a level that is non-toxic for primary neural cells [64].

Cellular compatibility, including cell adhesion and spreading, as well as cell interactions with nanofibers, were studied by direct plating onto meshes and examination via SEM. Fig. 5 shows that both 3T3 (Fig. 5E) and PC-12 (Fig. 5F) cells attached well and extended processes along fibers with all mesh types (representative images shown). PC-12 cells showed more extensive cellular aggregation compared to 3T3 cells, which is consistent with the differences seen when cells were grown on culture plastic.

3.8. In vivo implantation and tissue responses

3.8.1. In vivo changes in mesh appearance over time

For in vivo tissue compatibility studies, we implanted PM-10 (B1) and PM-0 (B1) under the skin of adult mice. We chose PM-10 because this mesh gave no loss in ultimate tensile strength or Young's modulus and its release of Mg^{2+} occurred in burst fashion. Mesh pieces were placed under the skin on the back of adult mice and animals were sacrificed after 3, 8 and 28 days in vivo (DIV). In histological sections of skin samples, shown in Fig. 6A–F, the meshes from 3 DIV showed the least amount of integration with adjacent connective tissues, as evidenced by the greatest degree of sporadic artifactual separation (Fig. 6A and B). By 28 DIV, there was a much greater degree of integration with adjacent tissues, as seen in Fig. 6E and F. Connective tissues around the meshes appeared thicker than in sham animals, so the meshes appeared to induce some generalized fibrosis, but the tissues did not show

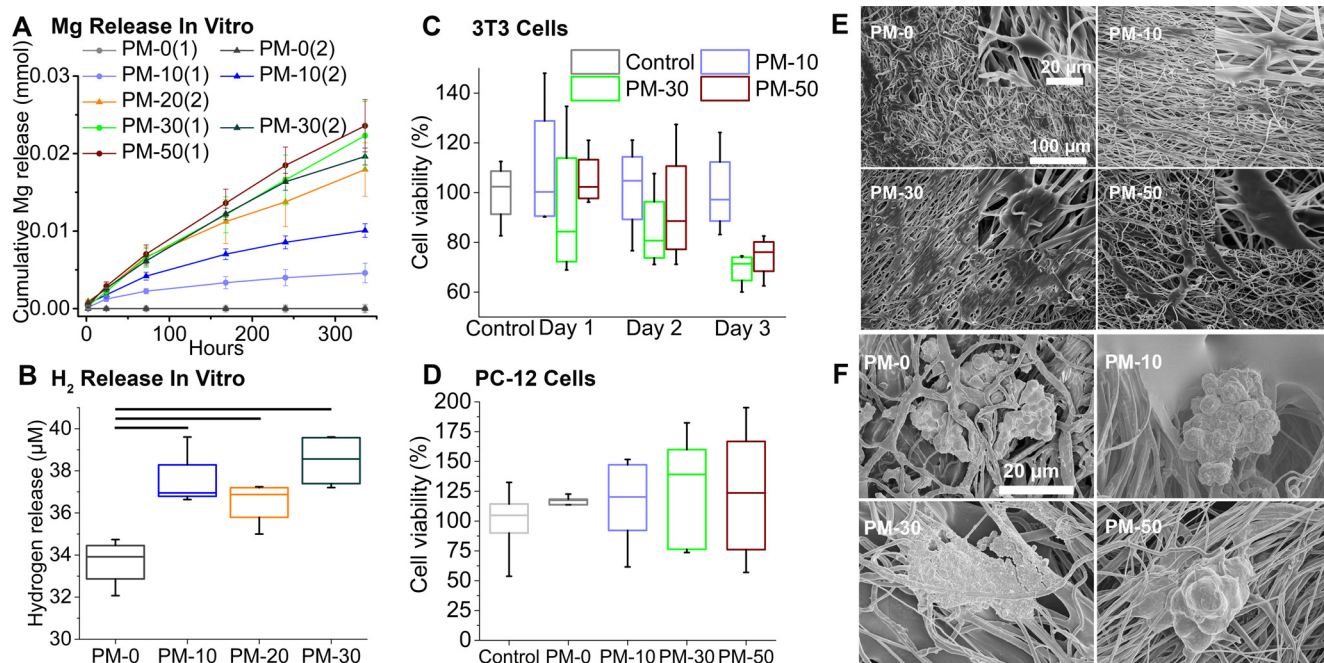


Fig. 5. Mesh performance in vitro and effects on viability, attachment and morphology of 3T3 and PC-12 cells. (A) Cumulative release of Mg^{2+} from meshes (B1 and B2) during immersion under cell culture conditions over 14 days (336 h). (B) H_2 content of medium from B2 meshes after a one-day incubation in basal culture medium, representative experiment. Bars show significant differences (ANOVA, $p = 0.011$, $n = 4$). (C) Viability of 3T3 fibroblasts cultured on meshes for 1, 2 and 3 days (Alamar Blue assay, data normalized to values for cells cultured on PM-0 mesh as the Control). Data are representative of multiple experiments (ANOVA, $p = 0.04$, but no pairs significant by post hoc, $n = 4$). (D) Viability of PC-12 cells grown on plastic for one day in mesh extracts or control medium (Alamar Blue assay, data normalized to cells in control medium without extracts, representative data set shown, ANOVA, $p = 0.6$, $n = 6$). SEM images of (E) 3T3 cells grown on mesh for 3 days and (F) PC-12 cells grown on mesh for 7 days.

dense deposits of collagen, as would be expected with detrimental fibrosis.

All PM-10 meshes were significantly thicker (apical to basal distance in cross section) than PM-0 at all time points (Fig. 6A–G). Thickness for both mesh types increased over time (Fig. 6G, two-way ANOVA, $p < 0.001$ for both group and time and all time points were different within mesh types). However, the rate of increase in thickness over time was the same for both types (Fig. 6G, parallel line analysis), suggesting that the presence of Mg differentially altered mesh thickness between 0 and 3 DIV, but did not differentially change the rate of thickness gain after that time point.

At 3 and 8 DIV, central areas of both mesh types contained a loose connective tissue, with strands of collagen and scattered cells (primarily leukocytes with some fibroblasts). The loose nature of these tissues often resulted in artifactual separation during sectioning. The spaces that were white (indicating a lack of tissue) and tissue areas (pink) were quantified using color thresholding in ImageJ. At 3 but not 8 DIV, the proportion of non-tissue “space” per central area examined (as %) was greater for PM-10 than PM-0 (Fig. 6H). These non-tissue spaces were presumably filled, in life, with air, extracellular fluid and/or PCL fibers. The PCL mesh dissolves during tissue processing, so fibers could not be differentiated from fluid or air in these sections.

To determine what might have influenced differential mesh thickness in vivo, dry meshes were imaged using confocal microscopy, thresholded with ImageJ and mesh thickness was measured (thresholded images shown in Fig. 6I and J). No difference was observed between PM-10 and PM-0 when dry (graph in Fig. 6K), which confirmed data from the materials characterization that the starting materials were equivalent. Mesh expansion could have occurred if exposure to physiological solutions caused Mg degradation and production of H_2 , which then resulted in swelling of nanofibers or increased space between nanofibers. To test this, meshes were immersed in cell culture medium with serum for 3 days in an

incubator and thickness was again measured. Both mesh types showed a trend towards increased thickness compared to dry (day 3 meshes were significantly thicker than dry PM-10), but PM-10 was not significantly thicker than the PM-0 (Fig. 6K). Individual fibers did not appear to have swollen, but this was not quantified. Thus, the presence of Mg appeared to cause mesh swelling only in vivo and not in vitro.

3.8.2. Macrophage infiltration

Over time in vivo, bands of closely apposed cells, which were composed primarily of macrophages, appeared at both apical and basal boundaries of implanted mesh (as determined by cell appearance in H&E, Fig. 6, or Masson’s trichrome, Fig. 7). These masses of presumably infiltrating cells took up a greater percentage of mesh area with increasing time in vivo (Fig. 7A–F, graph in G). At 3 DIV, the area taken up by these packed cells was small, around 20% of total mesh area, and there were no differences between PM-0 and PM-10 (Fig. 7A, B and G). At 8 DIV, the PM-10 meshes contained significantly more of these densely packed cells than PM-0 suggesting greater infiltration or greater expansion of the macrophage populations (Fig. 7C, D and G). At 28 DIV, all meshes were almost completely filled (>85% of mesh area) and no differences were seen between mesh types (Fig. 7E, F and G).

Signs of inflammation were observed inside and around the tissues. Inflammation was most apparent at 3 DIV, with reduction over time. Acute inflammation occurs after implantation of a foreign body due to the trauma of insertion and one characteristic is an initial increase in neutrophils in tissues that usually peaks at 2 DIV and then decreases due to neutrophil apoptosis. At both 3 and 8 DIV, the interior of the meshes, between the waves of infiltrating macrophages, had numerous cells that included both fibroblasts and leucocytes, indicating mild inflammation. To obtain a measure of inflammation, and because fibroblasts were a minority of the cells (determined by high power microscopy, not

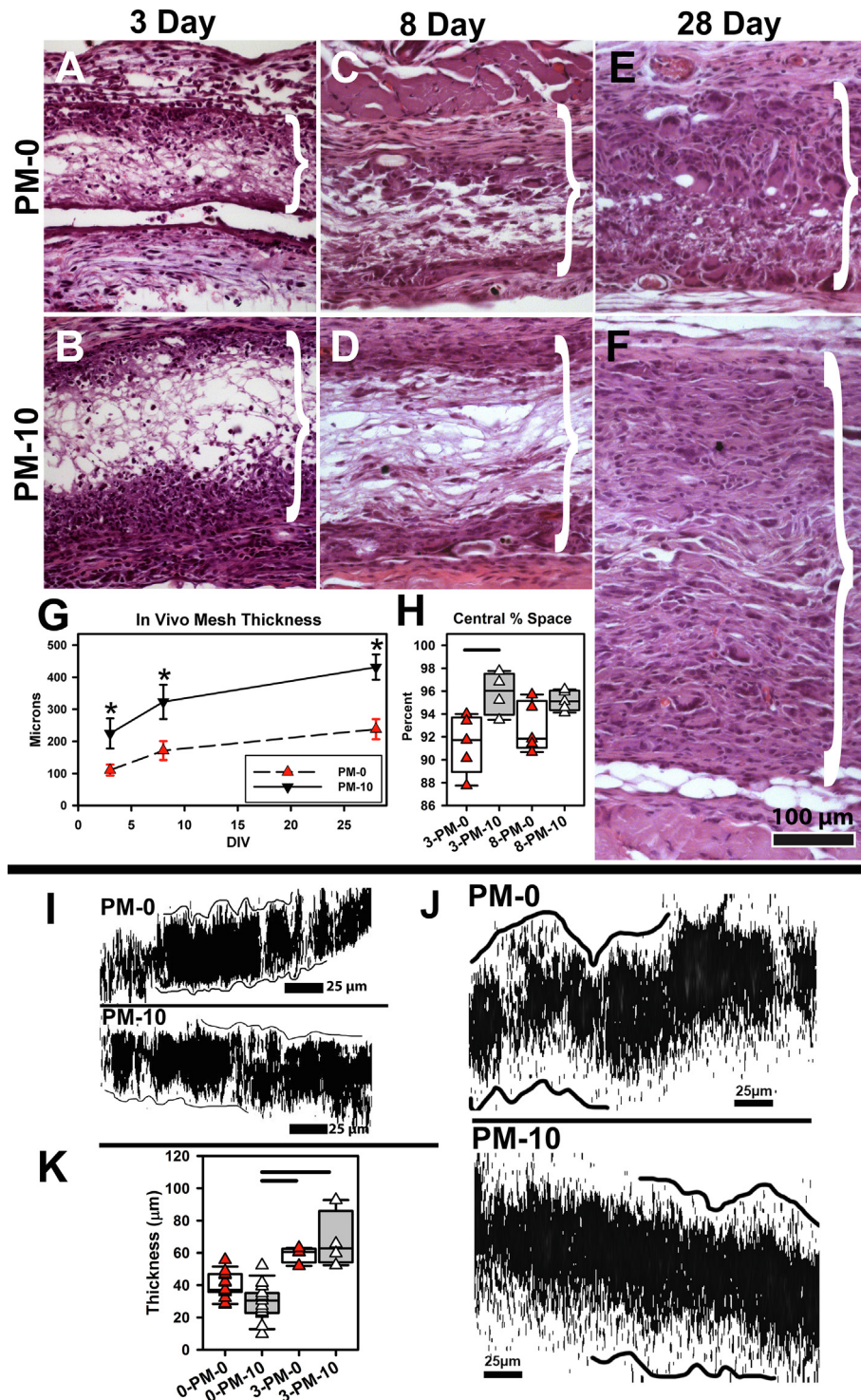


Fig. 6. Mesh thickness in vivo and in vitro. (A-F) In vivo, in H&E stained sections, PM-10 meshes were thicker than PM-0 at 3 DIV (A, B), 8 DIV (C, D) and 28 DIV (E, F). White brackets indicate mesh location within tissues. (G) The graph shows quantification of average thickness (two-way ANOVA, Group $p < 0.001$, $p = 0.1$ for interactions, $n = 4-5$, * show PM-10 to PM-0 differences, 25 measurements per image, 3 images per mouse). Slopes were not different by parallel line analysis, $p = 0.089$). (H) In H&E tissue sections, using color thresholding in ImageJ, spaces within meshes were analyzed (ANOVA, $p = 0.02$, $n = 4-5$, bars show differences, values expressed as a percent of total mesh area). (I-J) In vitro, mesh images when dry (I) and after immersion in culture medium for 3 days (J) were acquired using transmitted light on a confocal microscope and then thresholded using ImageJ, as shown. Apical-basal thickness was measured (examples of areas measured are outlined in I, J). (K) Thickness increased over time, but was not different between mesh types (ANOVA, $p < 0.001$, $n = 15$ and 4 for dry and 3 day measurements, respectively, bars show SDs).

quantified) nuclear numbers were counted within the loose connective tissue area. No significant differences were detected between PM-10 and PM-0, when nuclear numbers were expressed either as a percent of the area analyzed (Nuclear#/Area, Fig. 7H) or

as a percent of the actual tissue present (determined by thresholding) (Nuclear#/Tissue, Fig. 7I) (although 3 DIV PM-0 differed from 8 DIV PM-10). The lack of significant increases in nuclear density with PM-10 versus PM-0, per time point, suggests that the Mg

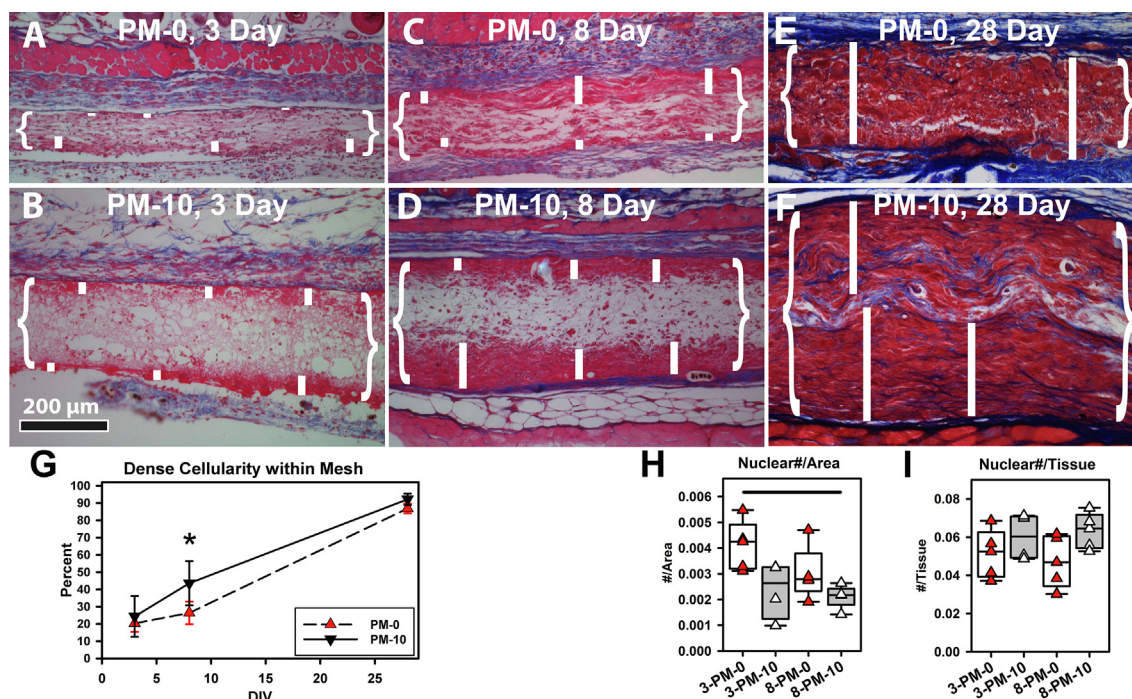


Fig. 7. Cellular ingrowth into mesh in vivo, after 3, 8 and 28 DIV. (A–F) In sections stained with Masson's Trichrome, which renders collagen blue and cells red, PM-0 meshes are shown at 3 (A), 8 (C) and 28 (E) DIV and PM-10 meshes are shown at 3 (B), 8 (D) and 28 (F) DIV. Brackets indicate localization of mesh and white bars represent the cellular ingrowth measurements used to generate the graph in G. (G) Graph of the dense cellularity (macrophages) as a percentage of total mesh area (two-way ANOVA, Group $p = 0.008$, $n = 4-5$, analysis as in Fig. 6G). (H, I) At 3 and 8 DIV, nuclear numbers in the central mesh areas were counted. (H) When nuclear density was calculated per image area examined, there were no differences between mesh types at either time point (ANOVA, $p = 0.03$, $n = 4-5$, bar shows only difference). (I) When nuclear density was calculated per the area covered by tissue within the same image area, there were no differences between mesh types (ANOVA, $p = 0.2$, $n = 4-5$). (For interpretation of the references to colour in this figure legend, the reader is referred to the web version of this article.)

did not induce greater tissue inflammation. Further characterization now requires biochemical analyses.

3.8.3. Macrophage polarization

Macrophage phenotype changes over time after tissue injury, from macrophages that stimulate inflammatory processes to ones that promote tissue repair [65,66]. To investigate macrophage phenotypes, we immunostained sections with antibodies to two macrophage polarization protein markers, inducible nitric oxide synthase (iNOS) and Arginase-1 (Arg1). iNOS is upregulated to a greater extent in macrophages that are at the M1 end of the macrophage polarization spectrum and pro-inflammatory. Arg1 is highly expressed by macrophages at the M2 (but not M1) end of the spectrum, which are macrophages that are less inflammatory and function to promote tissue repair [67,68]. Arg1 is an enzyme involved in the urea cycle, in producing ornithine, which is metabolized to proline, an essential protein in collagen formation. Ornithine can also be metabolized to form polyamines, which play roles in promoting cell proliferation and tissue regeneration [67].

At 3 DIV, PM-10 meshes did not differ from PM-0 meshes in iNOS expression, as determined by expressing area of iNOS as a percent of the area of DAPI (nuclear) staining within the mesh (Fig. 8A and C). In contrast, PM-10 meshes had significantly more Arg1 staining than PM-0 meshes (Fig. 8B and D). Comparing the two stains, PM-10 had a significantly higher Arg1/iNOS ratio (Fig. 8I). At 8 DIV, both mesh types showed more of each cell type compared to 3 DIV, but there were no differences between mesh types for iNOS, Arg1 or Arg1/iNOS (Fig. 8E–I). At 28 DIV (not shown), Arg-1 staining was reduced to near background levels in both mesh types. To be noted is that the iNOS antibody labels both nuclei and cytoplasm (Santa Cruz datasheet) while DAPI stains only nuclei, which explains how the iNOS percentages at 8 DIV were greater than 100% of DAPI area (Fig. 8G).

3.8.4. Mesh appearance at 28 DIV

To explore tissue differences at a time point when tissue remodeling would be occurring, we examined 28-day implantation. At sacrifice, mesh pieces (Fig. 9A, circles) were well vascularized, as seen by the fact that large blood vessels (Fig. 9A, arrowheads) were associated with the meshes and they appeared to connect meshes to adjacent subcutaneous fat pads (Fig. 9A, arrows). In sections, the meshes were almost completely filled with granuloma tissue that contained predominantly macrophages (Fig. 9B stained with H&E). This tissue was also filled with a large number of multinucleated foreign body giant cells (FBGCs, Fig. 9B, circles). The number of nuclei per cell varied and was often less than in the circled cells, but all cells with definite multiple nuclei were considered FBGCs for quantification. The relative percentages, sizes and densities were measured in H&E stained sections. However, there were no differences between PM-0 and PM-10 in the density of FBGCs within the meshes (Supplemental Fig. 5A, #/mm²) or the area covered with FBGC cytoplasm (as a percent of the fabric area, Supplemental Fig. 5B). The average size of FBGCs and the size of the largest FBGCs per fabric image were also not different between the mesh types (Supplemental Fig. 5C and D). Thus, by 28 DIV, the presence of Mg did not appear to result in a difference in FBGC number or size.

When 28 DIV sections were stained with Masson's trichrome stain (Fig. 9C and D), where collagen was colored blue and cell cytoplasm red, the amount of collagen per mesh area was greater with PM-10 versus PM-0 (Fig. 9E). The collagen was also more organized in PM-10 versus PM-0, as indicated by significantly longer continuous bands of collagen (white arrows in Fig. 9C and D, graph in Fig. 9F). Another measure of the foreign body reaction to an implanted material is the degree to which a foreign body is walled off from adjacent tissues with a fibrous capsule composed of dense collagen. Neither type of mesh had an average capsule

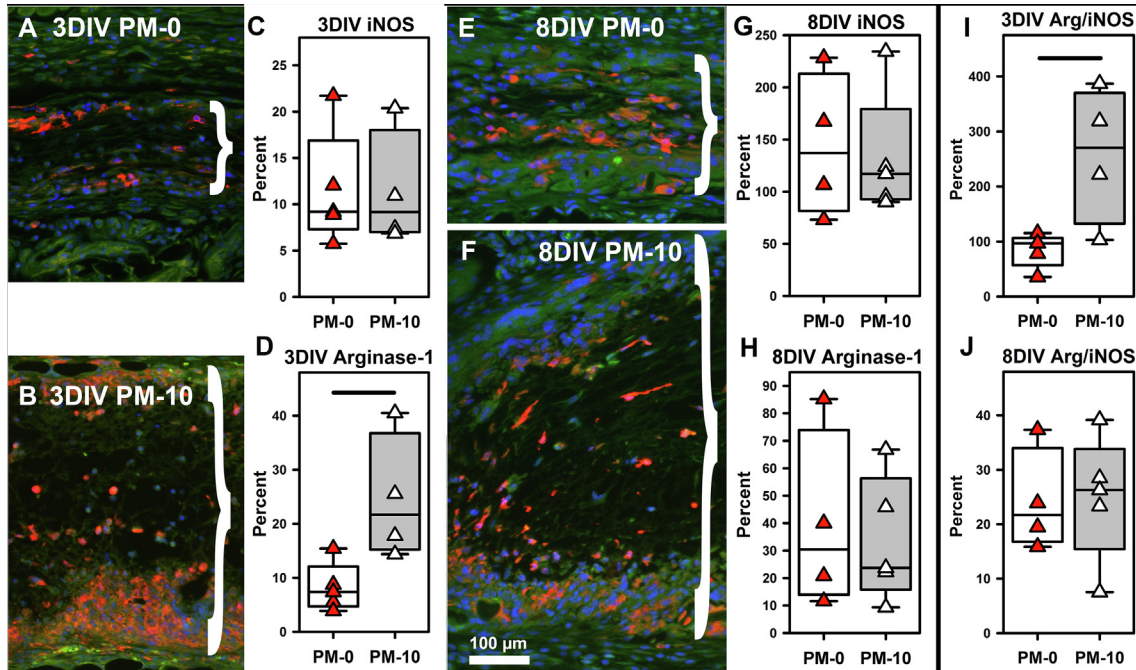


Fig. 8. Tissue sections of mesh immunostained for macrophage phenotypes. (A, B, E, F). Sections at 3 (A, B) and 8 DIV (E, F) were immunostained for iNOS (green) and Arg1 (red) and nuclei were stained with DAPI (blue) (brackets show meshes, bar = 100 μm, applies to all). Graphs (C, D, G, H) give stained area of each marker, as a percent of nuclear (DAPI+) area, within the mesh. The ratio of Arg1 to iNOS stained area is given as % for 3 (I) and 8 (J) DIV. Bars show significant differences (Rank sum tests, $p < 0.05$ only for (D) 3DIV Arg1 and (I) 3 DIV Arg1/iNOS, $n = 4-5$). (For interpretation of the references to colour in this figure legend, the reader is referred to the web version of this article.)

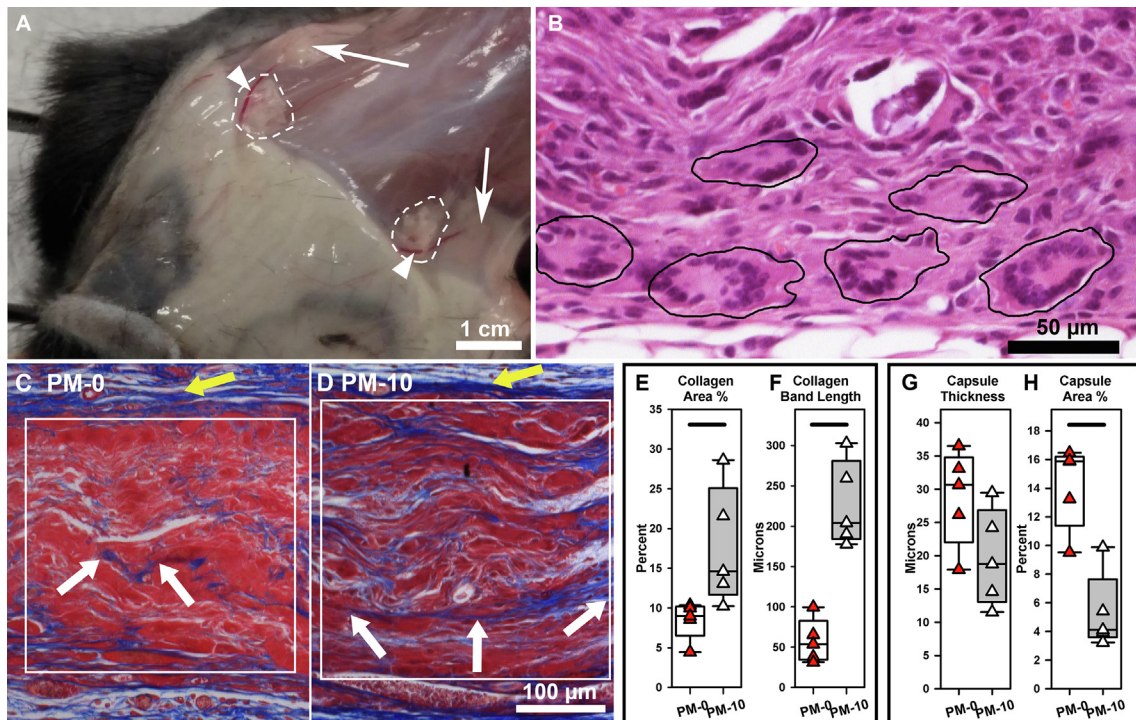


Fig. 9. In vivo tissues after 28 DIV. (A) At the 28 DIV sacrifice, the mesh pieces (inside white dashed circles) showed large blood vessels (white arrowheads) that appeared to interconnect mesh pieces and large lateral fat pads (white arrows). (B) In H&E stained sections, the mesh interior contained numerous macrophages and multinucleated FBGCs (FBGCs shown in black circles). (C, D) In sections stained with Masson's trichrome stain, measurements were made of the length of continuous collagen (blue) bands (white arrows), the percent of area covered by collagen (e.g., within the white squares, using color thresholding in ImageJ) and the thickness of the apical collagenous capsule (yellow arrows). (E, F) The (E) average length of continuous collagen bands and (F) area of collagen as a percent of the area examined were both significantly greater for PM-10 than PM-0 (Rank sum test, $p = 0.008$ and 0.016 , respectively, $n = 5$ mice per mesh type, averages of 36 fields total: 6 fields per image, 6 images per animal from 2 to 6 sections per animal). (G, H) In the same images, with a similar counting scheme, (G) capsule thickness in microns was not different between mesh types ($p = 0.095$), but if expressed (H) as a percent of mesh height, PM-10 capsules were significantly thinner than PM-0 ($p = 0.016$). (For interpretation of the references to colour in this figure legend, the reader is referred to the web version of this article.)

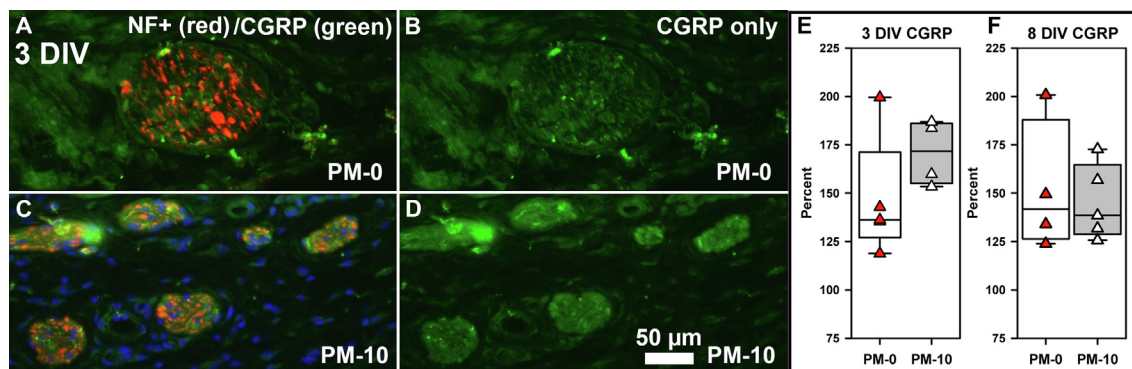


Fig. 10. CGRP Immunostaining in vivo. (A–D) Nerves in tissues apical and adjacent to mesh were immunostained for axons (NF, red), CGRP (green) and nuclei (blue) (3 DIV shown, with (A, C) merged CGRP and NF staining and (B, D) with just CGRP staining). (E, F) No differences were seen in CGRP staining intensity relative to background staining at either 3 or 8 DIV (Rank sum test, $p = 0.16$ and 1 , respectively, $n = 4–5$ mice per group, multiple sections examined per mouse, to allow multiple nerves to be measured, all averaged per mouse). Intensity of CGRP in NF-positive nerve fascicles was compared to intensity of neighboring connective tissue regions within the same nerve fascicle. (For interpretation of the references to colour in this figure legend, the reader is referred to the web version of this article.)

thickness greater than $35 \mu\text{m}$ (Fig. 9G), which can be considered relatively thin [69], and there were no differences between mesh types. However, if capsule thickness was expressed as a percent of mesh area then the PM-10 capsules were significantly thinner than the PM-0 capsules (Fig. 9H).

3.8.5. Calcitonin gene related peptide (CGRP) expression

A recent publication reported that Mg metal implants placed inside rat bones (femurs) stimulated increased CGRP expression in peripheral nerves adjacent to the bone, which was evident in immunostained sections [25]. This increase in CGRP led to increased bone density. To determine if there might be an effect of the PM-10 mesh on CGRP expression in adjacent nerve fibers, we immunostained for CGRP and for nerves, using an axonal marker, a neurofilament protein (Fig. 10A–D). We measured the intensity of immunostaining for CGRP in nerve fibers located apically, between the meshes and the overlying panniculus muscle layer, dermis and epidermis (using ImageJ). There were no differences between PM-10 and PM-0 meshes at either 3 or 8 DIV (Fig. 10E and F). This preliminary finding suggests no major influence of Mg on CGRP expression in nerve fibers in the skin.

4. Discussion

4.1. Electrospun mesh characterization

Electrospun PCL nanofiber meshes were made containing increasing amounts of Mg metal microparticles. Prior to electrospinning, the as-received Mg particle shapes were characterized by SEM and TEM, crystallinity by XRD, and hydrodynamic sizes by dynamic light scattering. The diffraction characteristics of the microparticles were consistent with those of pure Mg. The average size (hydrodynamic diameter) of the particles was distributed around 100 nm in number-weighted distributions and 1000 nm in volume-weighted distributions and this was consistent with high magnification images with SEM and TEM. These data indicate that the Mg particles had a wide size range, with most of them near the 100 nm size, but with some very big, which contributed heavily to shift the volume percent towards higher size values.

After electrospinning into meshes, electron microscopic images showed that the Mg particles were either embedded within individual PCL nanofibers or attached to the surface of fibers and coated with PCL. Mg presence was confirmed initially by EDS mapping. The nanofiber structure, where not obscured by attached Mg particles, was uniform and smooth. Analysis of nanofiber diame-

ters for Batch 1 meshes showed that the PM-30 and PM-50 meshes had a subset of fibers with higher diameters than in PM-0 or PM-10, but only PM-50 meshes had a higher average diameter, and only relative to PM-0 fibers. Increased fiber diameter is not likely to arise from the smaller metal particles (e.g., smaller than the fiber diameters), because such charged particles will result in a higher charge density on the ejected jet during spinning, which increases the stretching of the jet of polymer, and this creates smaller diameter fibers. Instead, it is more likely that the greater numbers of larger metal particles in the PM-50 mesh contributed to larger fiber diameters by hindering this “jet stretching”.

The porosity of the meshes, estimated using the calculated bulk density, did not differ between the mesh types. The range of porosity was between 60 and 70%, which is the preferred range for porosity of tissue engineering scaffolds [52]. Appropriate porosity is important for cellular adhesion and growth, as well as gas and nutrient exchange. Unlike consistently sized isotropic pores made by using particles or bubbles within a solidified polymer solution, the nanofiber mesh pores are the spaces formed when fibers cross randomly. The overall random 3D nature of the nanofiber mesh architecture mimics fibrous ECM better than solid cast materials, and this provides an advantage in its application as tissue engineering scaffolds.

To further confirm the presence of Mg in the meshes and to determine if the presence of Mg altered the chemistry of the PCL, meshes were examined using X-ray diffraction and FTIR. The XRD patterns suggest that with the PM-30 and PM-50 meshes, there was a decrease in the degree of crystallization of PCL. However, both the X-ray diffraction and FTIR spectra revealed no further changes and confirmed that the presence of Mg did not alter the chemical structure of the PCL. A similar lack of chemical interactions between Mg and polymer molecules has been reported previously, when Mg particles were added to poly-D-L-lactic acid composites [48]. The XRD analysis of the mesh also confirms that the Mg present in all fiber samples had the same crystallographic phases as the Mg metallic particles before electrospinning.

4.2. Mechanical properties of meshes

The presence of Mg significantly altered the mechanical properties of the nanofiber meshes. Even the smallest amount of Mg (PM-10) resulted in a distinctly lower ductility (lower ability to elongate with strain). However, the PM-10 mesh was not different from the PM-0 in ultimate tensile strength and Young’s modulus. Incremental addition of Mg beyond the PM-10 amount resulted in an incremental decrease in ultimate tensile strength and Young’s modulus.

The PM-50 was the most brittle and presented some difficulty in handling.

The mechanical properties of filler-reinforced polymer composites are determined primarily by the extent to which the filler material (in this case, Mg) becomes bonded to the polymer matrix and carries its share of the load [58]. When the filler material in a composite fibrous material carries the load, then the tensile strength is effectively unchanged with filler loading. When the filler is incapable of, or is less effective at, carrying the load, the strength decreases linearly with increased loading of filler material [59]. This latter effect is more pronounced (and may deviate from a linear correlation) with larger particle sizes, because the large particles effectively act as voids in the structure. Another factor is that the Mg particles were much stiffer than the PCL material and irregular in shape. It is known that fillers that are stiffer than the matrix, which therefore have a lower deformability and a shape that can interfere with the alignment of the parent material, can significantly alter any of the mechanical properties [60]. With our Mg meshes, the statistically similar ultimate tensile strength and Young's modulus values for PM-0 and PM-10 suggest that the particle loading in the PM-10 mesh did not significantly impact the load bearing properties of the mesh, but the higher content of Mg in the other mesh types did interfere.

Ductility was significantly altered by addition of any amount of Mg. This could have been due to interference of the large particles with elastic properties. When a polymer deforms, there is an elastic response, but the presence of large particles induces localized and diffused inelastic processes [7], which reduces the tensile strength as well as Young's modulus of composite nanofiber meshes. It is also true that elongation forces alter the crystalline phases in PCL [70] and having particles present will interfere with this crystallinity and therefore with all mechanical properties, including ductility. Predicting how mechanical properties are altered by the presence of Mg particles within PCL may only be fully understood with something like finite element analysis [58] or by analyzing mechanical strengths of single fibers. In our case, the high variability of both size and shape of the Mg particles make any such analysis difficult. Only if uniformity of size and shapes can be achieved will there be a possibility of predicting mechanical properties after adding specific amounts of Mg particles.

4.3. Mg ion release in vitro

Mg release from the meshes was determined by measuring the levels of free Mg^{2+} using a dye-based assay that involves a dye, Xylidyl blue, which changes color with increasing Mg^{2+} . Analysis of release showed that the PM-10 meshes, even though there were some differences between batches, both demonstrated a slowing of release by the end of 14 days, while all other mesh types continued to release at a steady rate. There were very few differences in the final cumulative release between the PM > 10 meshes, only that the PM-20 (B2) was different from the PM-50 (B1). These data are consistent with both the mechanical characteristics and the LM images that show that the PM-10 mesh appeared to lose all visible particles (Supplemental Fig. 4). This suggests that addition of the amount of Mg in PM-20 has reached or has almost reached a maximal amount. This may have to do with fiber size, as will be discussed below.

Batch differences were observed, but the direction of change was different for the PM-30 versus the PM-10 and was only significant with the PM-10 material. Further, the Mg release curves suggested that this didn't alter the fact that the PM-10 release was consistently different from the PM > 10 mesh release. Batch differences could be due to differential amounts of Mg becoming loosely attached during the electrospinning process, or perhaps due to differences in the amount of Mg suspended in the initial solution. Fur-

ther work is needed to characterize differences. There were two components to Mg^{2+} release, as demonstrated by the curves in Supplemental Fig. 3A. The Mg metal particles are small and the PCL is water permeable, so, theoretically, Mg degradation should occur very quickly upon contact with aqueous culture medium. High levels of release were seen initially, between 0 and 2 h, and then a reduced rate that was relatively constant thereafter, with some indication of an exponential decrease. The greater release over the first 2 h and the fact that release was somewhat batch-sensitive (Supplemental Fig. 3B), suggests that this initial release might have been due to rapid degradation of metal particles that were either very loosely attached, i.e., by entrapment within meshes, or covered by a very thin layer of PCL that loosened rapidly in aqueous solution. The relatively similar release per time point after ~2 h suggests that subsequent release was due to a steady rate of degradation of Mg from particles randomly dispersed under thicker layers of PCL. It is also possible that the PCL might be degrading over this time period, allowing even greater access of water to the Mg particles. PCL degradation is traditionally thought to take a much longer time than 14 days [71], but faster degradation could be occurring because the PCL was in thin nanofiber format. The PM-10 meshes showed a plateau phenomenon of release, with the rate of release decreasing over the last several days. As shown in Supplemental Fig. 3C, the rates of release calculated for the 240–336 h time period were much lower than the 0–2 h values, with a trend towards the PM-10 values being the lowest. This, plus the lower cumulative release of the PM-10 mesh types is consistent with the LM images, as discussed above. However, if this indicates that Mg particle degradation was essentially complete by 14 days in vitro and all meshes have the same size Mg particles, then why didn't the PM > 10 meshes plateau also? This might be explained by examining the histograms of mesh fiber diameters, as shown in Fig. 3. The PM-30 and -50, but not PM-10 or -0, meshes contained a subset of larger fibers (>3 μm diameter). Larger diameter fibers would take longer to allow water to diffuse in and Mg^{2+} to diffuse out, so they would continue to release Mg^{2+} after Mg particles were gone from the smaller fibers. This suggests, for future studies, that it might be possible to tailor the release of Mg^{2+} over a period of days to weeks by designing different thickness fibers. Given that Mg^{2+} have multiple beneficial effects, this has a broad appeal for clinical applications.

4.4. Hydrogen release in vitro

Analysis of the hydrogen release in physiological solution showed that meshes containing Mg particles did release H_2 . The H_2 measurements had to account for several factors. First was the high diffusibility of hydrogen gas. Culture flasks had to remain closed during incubation, which limited the period of study to avoid depletion of CO_2 and a rise in pH of this medium (occurs even without cells). Measurements across the 3 min time period were averaged to account for movement artifacts and the decline in current due to release of H_2 when the flask was opened to insert the electrode. The short time period and variability most likely explain why no differences were seen between mesh types. Finally, because developing a standard curve required continual stirring to dissolve H_2 , serum had to be avoided. Future studies will address these factors.

Studies of the potential therapeutic effects of molecular hydrogen are increasing in number. H_2 in cell culture medium was shown to be an anti-oxidant that reacts only with hydroxyl ($\cdot OH$) and peroxynitrite ($ONOO^-$) ions, but not with other reactive oxygen species [38]. In vivo, this antioxidant effect could potentially reduce excessive oxidative stress, which is a factor in aging and cancer [72]. Therapeutically, H_2 , consumed by gas inhalation, hydrogenated water ingestion or hydrogenated saline injection

has shown protective effects in preclinical disease models and in some promising clinical trials for disorders that include diabetes and Parkinson's Disease [35,73]. In future studies, it would be interesting to see if the small amount of H₂ produced by the mesh can generate effects on cultured cells. Similar H₂ concentrations (around 30 to 40 μM), provided protection for cultured PC-12 cells in an oxidative environment [38].

4.5. Cell cytocompatibility in vitro

For both 3T3 cells and PC-12 cells, no loss of cell viability was seen with any mesh type. Possible primary toxicants in these nanofibers were anticipated to be leached chemicals remaining from synthesis, but excessive levels of released Mg²⁺ can also be cytotoxic. Research has shown that the concentration of Mg²⁺ that reduces cell viability significantly (i.e. <75%) is ~15–20 mM in many cell types [64,74–76]. Some types of primary bone derived cells can survive in 100 mM, but show decreased cell function above 20 mM [24]. The Mg release was determined for the PC-12 cell assay (data not shown) and the levels were well below a potentially toxic level. Our results indicate that these fibers were not releasing anything that was toxic to cells.

4.6. In vivo implantation and tissue responses

Tissue reactions to implanted biomaterials include 1) wound healing initiated by the innate immune response and 2) a reaction to the biomaterial, called the foreign body response (FBR) [72,73]. The FBR includes absorption of proteins on the implant, attraction of immune cells, their attachment to or penetration into the foreign body, formation of a granulation tissue comprised of fibroblasts, macrophages and newly formed blood vessels and activation of macrophages to degrade the foreign material. If the material is resistant to early degradation, macrophages can fuse to form foreign body giant cells (FBGCs) [72]. If the material persists, with or without chronic inflammation, fibroblasts wall off the material with a collagenous capsule. The extent of encapsulation increases if the material is irritating or toxic to tissues. We examined these aspects of tissue response with in vivo implantation studies.

4.7. Mesh thickness in vivo

Our data showed a significant increase in mesh size over time and a difference with the addition of Mg that appears to have occurred during the first three days after implantation. Our in vitro studies suggest that the differential changes with Mg were not an intrinsic property of the mesh alone, as there were no differential changes in mesh thickness upon immersion in a physiological solution at body temperature. In vivo, we speculate that the differential expansion arose because the pressure from H₂ production was prevented from escaping as rapidly as it could in vitro, because of the tissues surrounding the mesh in vivo. Therefore, the gas pressure may have pushed nanofibers aside and expanded the total mesh area. This is consistent with the observation of a greater percentage of "space" (areas without tissue) in the 3 DIV PM-10 mesh (Fig. 6H). At time points after 3 DIV, there were no further differential increases in the thickness of PM-10 versus PM-0, although both increased in thickness with time. A lack of differential change after 3 DIV could have been caused by slower H₂ production, as the Mg pieces degraded or were even completely degraded. The continued increase in thickness over time of both mesh types was presumably due to continued cellular ingrowth, which we demonstrated.

4.8. Tissue inflammatory status

An alternative explanation as to why the PM-10 mesh increased in size relative to the PM-0 by 3 DIV is that the PM-10 fabric underwent greater fluid retention i.e., edema. This would occur if the Mg presence caused tissue irritation initially. We cannot rule out this latter possibility completely but, our observation was that the total cell count within the center of the meshes was similar between PM-10 and PM-0 at 3 and 8 DIV. While not definitive, this finding argues against a significant increase in tissue inflammation due to the Mg. At 3 DIV, there were signs of mild inflammation both inside and around the tissues and these accumulations decreased over time after 3 DIV. We did not see any evidence of an increase in inflammatory status at 28 DIV. Our measure of inflammation (nuclear counts) was only a preliminary analysis and further characterization of the inflammatory status will require additional assays.

4.9. Macrophage phenotypes

The time course of appearance of M1 and M2 macrophages differs during wound healing, with numbers distributed in bell curves [77]. M1 macrophage numbers peak around 3 days after injury, at which time the transition to M2 phenotypes begins. M2 numbers reach levels comparable to M1 cells at around 7 days after injury and reach a crest at about 10 days after injury [77]. Based on this time scale and the changes that we see over time, the presence of Mg in PCL mesh stimulated an earlier increase in the appearance of M2 macrophages.

As stated previously, in wound healing and reactions to foreign bodies like implants, M1 macrophages (classically activated) differ in function from M2 macrophages (alternatively-activated) and are at two ends of a polarization spectrum of macrophage phenotypes, with the capacity to do phenotypic switching [65,66]. M1-like macrophages are activated by specific cytokines to produce an acute immune reaction that includes release of reactive oxidative species and attraction of neutrophils to the site to remove foreign material [78,79]. These activities perform important functions in early wound healing but if prolonged, can be harmful, i.e., stimulating chronic inflammation, overly rapid degradation of an implant, creation of a dense fibrous capsule and/or scar formation [65,66]. M2 macrophages, activated by different cytokines, stimulate fibroblast migration into the affected area, fibroblast secretion of collagen, increased production of blood vessels and production of ornithine and polyamines that further promote cell growth and tissue repair; they also inhibit inflammation and fibrosis, overall resulting in tissue remodeling and repair [80–82].

In tissue engineering, modulating an implanted material to stimulate an increased appearance of M2 macrophages at earlier time points is correlated with greater tissue acceptance and medical success of implants [65,66,83,84]. For example, incorporation of the cytokine IL-4, which increases M2 macrophage differentiation, into surgical meshes, increased early M2 numbers and, later, decreased fibrous capsule thickness, increased collagen deposition and improved mesh biocompatibility [69]. We propose that incorporating Mg metal into nanofiber meshes is similarly improving the tissue responses compared to PCL material alone. The Mg presence stimulated greater amounts of M2 macrophages at earlier time points, increased macrophage infiltration into the meshes (suggesting increased macrophage motility or activity) at 8 DIV and increased collagen production at 28 days. Further effects on biocompatibility will focus on examining more time points, including later ones to determine effects on scarring after the meshes are completely degraded. In addition, because the spectrum of macrophage polarization is much more complex than just M1 and M2 macrophages [85,86], future work is needed to fully analyze

macrophage subtypes in the tissue response. However, the effects we see suggest a role for Mg metal in reducing tissue reactions to other implanted materials.

4.10. 28 DIV collagen and capsule

As the FBR to most biomaterials proceeds, macrophages are replaced by infiltrating fibroblasts laying down ECM proteins, like collagen, and this collagen gets organized into bands to eventually form scar tissue. Collagen bands serve a useful purpose in damaged tissue to hold the tissue together while remodeling occurs. Thus, more ECM and a greater degree of organization of the ECM during tissue reorganization are signs of improved resolution of the FBR and are desirable traits in a connective tissue area like the dermis of the skin [83]. This is what our 28 DIV data suggest, that the presence of Mg particles has a long-lasting effect that increases tissue remodeling, a process that is designed to return the tissue to normal connective tissue. This is consistent with other studies where Mg metal added to a composite polymer induced greater secretion of fibronectin (another ECM protein) by mesenchymal stem cells in vitro [48]. It is also consistent with the early increase in Arginase 1 activity of macrophages, which should contribute to increased collagen formation.

The relatively thin capsules suggest low irritation of both mesh types, which is consistent with the fact that PCL is an FDA-approved biomaterial with a generally accepted low tissue irritation capacity. However, clinically, as with surgical meshes, there is always room to further improve tissue acceptance because, as PCL degrades, it releases acidic compounds that can cause tissue irritation. Data in the literature also suggest that increasing the size of fibers (while remaining near the nanoscale) and increasing the degree of alignment might also improve biocompatibility and reduce the FBR to the meshes [87,88].

The fact that the numbers and sizes of the FBGCs within the meshes at 28 DIV were not different between the mesh types (Supplemental Fig. 5) is consistent with the idea that there might not be any Mg remaining in the meshes at 28 DIV. Thus, the only factor influencing FBGCs would be the PCL, which should not have degraded significantly by this point. FBGCs are a sign that the foreign material is still present and resistant to removal by normal macrophage activity. We further speculate that even if Mg particles remained, they might not stimulate FBGC formation, because the metal particles might be small enough to be taken up into mononuclear macrophages and readily digested. Overall, the 28 DIV observations suggest that adding Mg metal particles to PCL mesh at the level in PM-10, had a positive influence that was effective through 28 DIV at promoting tissue healing and also at reducing (but not eliminating) the FBR to PCL.

An alternative hypothesis to explain the in vivo differences is that these were caused by the changes in mesh mechanical properties with Mg metal addition. The stiffness of implants can modify macrophage polarization, as shown by altering stiffness of collagen matrices or hydrogels [89,90]. Elastic modulus is the most critical parameter to determine the stiffness of a biomaterial [91], which is indicated by the Young's modulus. Based on our data (Fig. 4B), the Young's modulus was not significantly different between PM-0 and PM-10 meshes, suggesting that stiffness was probably not a factor influencing macrophage phenotype in our implants. Another factor could be the topographic properties of the meshes. Studies have shown that factors such as pore size and/or spacing between fibers and diameter of fibers can affect macrophage phenotypes [92–94]. In terms of porosity, the PM-0 and PM-10 meshes did not differ in porosity. In terms of nanofiber diameter of electrospun meshes, Sanders et al. showed an increase in fibrous capsule thickness with polymer fiber diameters of 6–15 μm compared to <5 μm , which led them to declare that fiber diameters <5 μm

resulted in minimal tissue reactivity [95]. In our studies, all fiber diameters were <5 μm and only the PM-50 mesh showed a significant difference from PM-0. Thus, because all physical differences were minimal, we do not believe that the mesh stiffness, porosity or nanofiber diameters were influencing the cellular responses.

Beneficial effects on tissue responses, including altering macrophage phenotype, have been reported previously after Mg metal was added to other implant materials. Whether Mg metal was incorporated into a solid polymer, added as metal particles to cultured cells or doped into titanium metal, studies have shown that several types of cultured cells decreased production of pro-inflammatory cytokines or increased gene or protein expression of molecules involved in tissue repair [48,49,96,97]. When such materials were implanted in vivo, they stimulated increased M2 macrophage polarization, reduced thickness of fibrous capsules and decreased surrounding inflammation, compared to the same materials without Mg [49,97]. Thus, Mg metal presence, either in vitro or in vivo, alters macrophage polarization, is generally anti-inflammatory and can improve tissue acceptance of a co-implanted material. Our data are a further demonstration that the presence of Mg can have beneficial modulatory effects on tissue responses to an implanted biomaterial.

4.11. CGRP

The differences between our findings of no effect on CGRP expression and the previous report of Mg metal implants causing increased CGRP [25] could be due to multiple factors. While both studies examined protein expression via immunostaining, we did not confirm our findings with quantitative assays, e.g. via ELISAs. The size of the implant could have made a difference. In the Zhang study, they inserted a metal rod into a rat bone, which meant that they had significantly more metal per animal than we had with Mg incorporated into a mesh. Another consideration is that CGRP is a known anabolic stimulant for bone formation [25], but is not thought to be anabolic for connective tissue metabolism. Thus, peripheral nerves around bone might be more sensitive to Mg^{2+} than those under the skin, because Mg^{2+} plays a more significant role in bone metabolism than in connective tissue metabolism.

4.12. Clinical relevance

Our findings might lead to clinical applications with respect to, first, providing both anti-inflammatory and neuroprotective effects after nervous tissue injury. Our previous work has shown beneficial effects of Mg metal filaments in repairing peripheral nerves [40]. To augment and expand this, placing Mg metal particles in the conduit might provide a greater degree of initial neuroprotection, because smaller particles would degrade more rapidly than the metal filaments, therefore releasing greater amounts of Mg^{2+} at earlier time points.

Another potential clinical use for adding Mg metal would be to reduce inflammation of surgical materials already in use. This includes staples, sutures or surgical meshes made of polymers similar to PCL. All of these can cause varied degrees of inflammation and using them clinically requires an understanding of the risks versus the benefits [79]. Addition of micro-sized Mg metal particles might provide a means to reduce these inflammatory effects and improve the clinical benefits of these surgical materials.

5. Conclusion

The objective of this work was to synthesize a biomaterial scaffold, through a process that would be comparatively easy and inexpensive to scale up and that has structural and material properties

that are beneficial for tissue engineering applications. We designed and fabricated biodegradable Mg/PCL composite nanofiber meshes using electrospinning technology. Incorporation of Mg caused no change in the chemical structure of the PCL fibers, but changed the tensile properties; most notably breaking strain decreased with increasing Mg. During in vitro immersion tests, meshes with Mg released H₂, and Mg ion release was proportional to Mg content. The viability of 3T3 and PC-12 cells in culture was not decreased by contact with or extracts from the meshes with Mg. When implanted subcutaneously in mice, the presence of Mg metal resulted in an early increase in the size of the mesh, which may have arisen due to trapped H₂, released by Mg degradation. Then, Mg/PCL meshes showed significant improvements in tissue repair over PCL mesh alone. Meshes with Mg stimulated an earlier appearance of tissue reparative macrophages, an increase in the rate of macrophage infiltration into the mesh and, at later times, increased collagen deposition and collagen organization, all of which are indications that the Mg/PCL was improving tissue healing over PCL alone. Thus, our observations suggest that adding Mg to another biomaterial during electrospinning is a way to alter the tissue reactions to the original biomaterial, which is consistent with previous reports of additions to other, non-electrospun materials. Our results add to a body of work that suggests that the inclusion of Mg metal could improve the success of many types of tissue engineering approaches to biomedical repairs.

Acknowledgements

This work is supported financially by the National Science Foundation, through the Engineering Research Center for Revolutionizing Metallic Biomaterials (ERC-RMB, EEC-0812348) and by a grant from the University of Cincinnati Dept. of Orthopaedic Surgery. We thank Dr. Keith Stringer, University of Cincinnati College of Medicine, Dept. of Pathology and Lab Medicine, for input on in vivo interpretations. We thank Li Cai Haney, Jacob Korniak, Nuthara Jayasinghe, Elizabeth Norwood and John Asiruwa, University of Cincinnati, for their technical assistance. We thank Dr. Sergey Yarmolenko, Dr. Zhigang Xu, Dr. Svitlana Fialkova, Dr. Boyce Collins and Sheikh Saudi, North Carolina A&T State University, NSF ERC-RMB and Dept. of Mechanical Engineering for their technical assistance to characterize nanofiber meshes. Characterization of meshes was performed in part at the Joint School of Nanoscience and Nanoengineering, a member of the Southeastern Nanotechnology Infrastructure Corridor and National Nanotechnology Coordinated Infrastructure (NSF ECCS-1542174).

Disclosures

None of the authors have financial disclosures to report.

Appendix A. Supplementary data

Supplementary data to this article can be found online at <https://doi.org/10.1016/j.actbio.2019.04.061>.

References

- [1] A. Greiner, J.H. Wendorff, Electrospinning: a fascinating method for the preparation of ultrathin fibers, *Angew. Chem. Int. Ed.* 46 (2007) 5670–5703, <https://doi.org/10.1002/anie.200604646>.
- [2] R. Vasita, D.S. Katti, Nanofibers and their applications in tissue engineering, *Int. J. Nanomed.* 1 (2006) 15–30, <https://doi.org/10.2147/nano.2006.1.1.15>.
- [3] Y. Wang, G. Wang, L. Chen, H. Li, T. Yin, B. Wang, J.C.-M. Lee, Q. Yu, Electrospun nanofiber meshes with tailored architectures and patterns as potential tissue-engineering scaffolds, *Biofabrication* 1 (2009), <https://doi.org/10.1088/1758-5082/1/1/015001>.
- [4] X. Wang, B. Ding, B. Li, Biomimetic electrospun nanofibrous structures for tissue engineering, *Mater. Today* 16 (2013) 229–241, <https://doi.org/10.1016/j.mattod.2013.06.005>.
- [5] S.Y. Chew, J. Wen, E.K.F. Yim, K.W. Leong, Sustained release of proteins from electrospun biodegradable fibers, *Biomacromolecules* 6 (2005) 2017–2024, <https://doi.org/10.1021/bm0501149>.
- [6] E.-R. Kenawy, G.L. Bowlin, K. Mansfield, J. Layman, D.G. Simpson, E.H. Sanders, G.E. Wnek, Release of tetracycline hydrochloride from electrospun poly(ethylene-co-vinylacetate), poly(lactic acid), and a blend, *J. Control. Release* 81 (2002) 57–64, [https://doi.org/10.1016/S0168-3659\(02\)00041-X](https://doi.org/10.1016/S0168-3659(02)00041-X).
- [7] S. Maretschek, A. Greiner, T. Kissel, Electrospun biodegradable nanofiber nonwovens for controlled release of proteins, *J. Control. Release* 127 (2008) 180–187, <https://doi.org/10.1016/j.jconrel.2008.01.011>.
- [8] H. Nie, C.-H. Wang, Fabrication and characterization of PLGA/HAp composite scaffolds for delivery of BMP-2 plasmid DNA, *J. Control. Release* 120 (2007) 111–121, <https://doi.org/10.1016/j.jconrel.2007.03.018>.
- [9] J. Sharma, M. Lizu, M. Stewart, K. Zygula, Y. Lu, R. Chauhan, X. Yan, Z. Guo, E.K. Wujcik, S. Wei, Multifunctional nanofibers towards active biomedical therapeutics, *Polymers (Basel)* 7 (2015) 186–219, <https://doi.org/10.3390/polym7020186>.
- [10] C. Ball, E. Krogstad, T. Chaowanachan, K.A. Woodrow, Drug-eluting fibers for HIV-1 inhibition and contraception, *PLoS One* 7 (2012), <https://doi.org/10.1371/journal.pone.0049792>.
- [11] S.-F. Chou, D. Carson, K.A. Woodrow, Current strategies for sustaining drug release from electrospun nanofibers, *J. Control. Release* 220 (2015) 584–591, <https://doi.org/10.1016/j.jconrel.2015.09.008>.
- [12] E.J. Falde, J.D. Freedman, V.L.M. Herrera, S.T. Yohe, Y.L. Colson, M.W. Grinstaff, Layered superhydrophobic meshes for controlled drug release, *J. Control. Release* 214 (2015) 23–29, <https://doi.org/10.1016/j.jconrel.2015.06.042>.
- [13] E.A. Krogstad, K.A. Woodrow, Manufacturing scale-up of electrospun poly(vinyl alcohol) fibers containing tenofovir for vaginal drug delivery, *Int. J. Pharm.* 475 (2014) e282–e291, <https://doi.org/10.1016/j.ijpharm.2014.08.039>.
- [14] J.J. Stankus, D.O. Freytes, S.F. Badylak, W.R. Wagner, Hybrid nanofibrous scaffolds from electrospinning of a synthetic biodegradable elastomer and urinary bladder matrix, *J. Biomater. Sci. Polym. Ed.* 19 (2008) 635–652, <https://doi.org/10.1163/156856208784089599>.
- [15] N. Cai, C. Li, C. Han, X. Luo, L. Shen, Y. Xue, F. Yu, Tailoring mechanical and antibacterial properties of chitosan/gelatin nanofiber membranes with Fe₃O₄ nanoparticles for potential wound dressing application, *Appl. Surf. Sci.* 369 (2016) 492–500, <https://doi.org/10.1016/j.apsusc.2016.02.053>.
- [16] K. Ghosal, C. Agatemor, Z. Spítálský, S. Thomas, E. Kny, Electrospinning tissue engineering and wound dressing scaffolds from polymer-titanium dioxide nanocomposites, *Chem. Eng. J.* 358 (2019) 1262–1278, <https://doi.org/10.1016/j.cej.2018.10.117>.
- [17] H.S. Sofi, R. Ashraf, A.H. Khan, M.A. Beigh, S. Majeed, F.A. Sheikh, Reconstructing nanofibers from natural polymers using surface functionalization approaches for applications in tissue engineering, drug delivery and biosensing devices, *Mater. Sci. Eng. C* 94 (2019) 1102–1124, <https://doi.org/10.1016/j.msec.2018.10.069>.
- [18] A. Suryavanshi, K. Khanna, K.R. Sindhu, J. Bellare, R. Srivastava, Magnesium oxide nanoparticle-loaded polycaprolactone composite electrospun fiber scaffolds for bone-soft tissue engineering applications: in-vitro and in-vivo evaluation, *Biomed. Mater.* 12 (2017), <https://doi.org/10.1088/1748-605X/aa792b>.
- [19] C. Han, N. Cai, V. Chan, M. Liu, X. Feng, F. Yu, Enhanced drug delivery, mechanical properties and antimicrobial activities in poly(lactic acid) nanofiber with mesoporous Fe₃O₄-COOH nanoparticles, *Colloids Surfaces A Physicochem. Eng. Asp.* 559 (2018) 104–114, <https://doi.org/10.1016/j.colsurfa.2018.09.012>.
- [20] B.J.C. Luthringer, F. Feyerabend, R. Willumeit-Römer, Magnesium-based implants: a mini-review, *Magnes. Res.* 27 (2014) 142–154, <https://doi.org/10.1684/mrh.2015.0375>.
- [21] D. Zhao, F. Witte, F. Lu, J. Wang, J. Li, L. Qin, Current status on clinical applications of magnesium-based orthopaedic implants: a review from clinical translational perspective, *Biomaterials* 112 (2017) 287–302, <https://doi.org/10.1016/j.biomaterials.2016.10.017>.
- [22] J.A. Cowan, Structural and catalytic chemistry of magnesium-dependent enzymes, *Biometals* 15 (2002) 225–235, <https://doi.org/10.1023/A:1016022730880>.
- [23] P. Sharma, C. Chung, M. Vizcaychipi, Magnesium: the neglected electrolyte? a clinical review, *Pharmacol. Pharmacy, Pharmacol. Pharm.* 5 (2014) 762–772, <https://doi.org/10.4236/pp.2014.57086>.
- [24] S. Yoshizawa, A. Brown, A. Barchowsky, C. Sfeir, Magnesium ion stimulation of bone marrow stromal cells enhances osteogenic activity, simulating the effect of magnesium alloy degradation, *Acta Biomater.* 10 (2014) 2834–2842, <https://doi.org/10.1016/j.actbio.2014.02.002>.
- [25] Y. Zhang, J. Xu, Y.C. Ruan, M.K. Yu, M. O’Laughlin, H. Wise, D. Chen, L. Tian, D. Shi, J. Wang, S. Chen, J.Q. Feng, D.H.K. Chow, X. Xie, L. Cheng, L. Huang, S. Huang, K. Leung, N. Lu, L. Zhao, H. Li, D. Zhao, X. Guo, K. Chan, F. Witte, H.C. Chan, Y. Zheng, L. Qin, Implant-derived magnesium induces local neuronal production of CGRP to improve bone-fracture healing in rats, *Nat. Med.* 22 (2016) 1160–1169, <https://doi.org/10.1038/nm.4162>.
- [26] M. Rondanelli, A. Opizzi, F. Monteferrario, N. Antonello, R. Manni, C. Klersy, The effect of melatonin, magnesium, and zinc on primary insomnia in long-term care facility residents in Italy: a double-blind, placebo-controlled clinical trial, *J. Am. Geriatr. Soc.* 59 (2011) 82–90, <https://doi.org/10.1111/j.1532-5415.2010.03232.x>.

- [27] A.A. Yousef, A.E. Al-Deeb, A double-blinded randomised controlled study of the value of sequential intravenous and oral magnesium therapy in patients with chronic low back pain with a neuropathic component, *Anaesthesia* 68 (2013) 260–266, <https://doi.org/10.1111/anae.12107>.
- [28] K. Brandao, F. Deason-Towne, A.-L. Perraud, C. Schmitz, The role of Mg²⁺ in immune cells, *Immunol. Res.* 55 (2013) 261–269, <https://doi.org/10.1007/s12026-012-8371-x>.
- [29] B. Chaigne-Delalande, M.J. Lenardo, Divalent cation signaling in immune cells, *Trends Immunol.* 35 (2014) 332–344, <https://doi.org/10.1016/j.it.2014.05.001>.
- [30] J.H. de Baaij, J.G. Hoenderop, R.J.M. Bindels, Magnesium in man: Implications for health and disease, *Physiol. Rev.* 95 (2015) 1–46, <https://doi.org/10.1152/physrev.00012.2014>.
- [31] R. Vink, Magnesium in the CNS: recent advances and developments, *Magnes. Res.* 29 (2016) 95–101, <https://doi.org/10.1684/mrh.2016.0408>.
- [32] I. Slutsky, N. Abumaria, L.-J. Wu, C. Huang, L. Zhang, B. Li, X. Zhao, A. Govindarajan, M.-G. Zhao, M. Zhuo, S. Tonegawa, G. Liu, Enhancement of learning and memory by elevating brain magnesium, *Neuron* 65 (2010) 165–177, <https://doi.org/10.1016/j.neuron.2009.12.026>.
- [33] W. Li, J. Yu, Y. Liu, X. Huang, N. Abumaria, Y. Zhu, X. Huang, W. Xiong, C. Ren, X.-G. Liu, D. Chui, G. Liu, Elevation of brain magnesium prevents synaptic loss and reverses cognitive deficits in Alzheimer's disease mouse model, *Mol. Brain.* 7 (2014) 65, <https://doi.org/10.1186/s13041-014-0065-y>.
- [34] G. Liu, J.G. Weinger, Z.-L. Lu, F. Xue, S. Sadeghpour, Efficacy and safety of MMFS-01, a synapse density enhancer, for treating cognitive impairment in older adults: a randomized, double-blind, placebo-controlled trial, *J. Alzheimer's Dis.* 49 (2015) 971–990, <https://doi.org/10.3233/JAD-150538>.
- [35] S. Ohta, Molecular hydrogen as a novel antioxidant: overview of the advantages of hydrogen for medical applications, *Methods Enzymol.* 555 (2015) 289–317, <https://doi.org/10.1016/j.mbs.2014.11.038>.
- [36] K. Fujita, T. Seike, N. Yutsudo, M. Ohno, H. Yamada, H. Yamaguchi, K. Sakumi, Y. Yamakawa, M.A. Kido, A. Takaki, T. Katafuchi, Y. Tanaka, Y. Nakabeppu, M. Noda, Hydrogen in drinking water reduces dopaminergic neuronal loss in the 1-methyl-4-phenyl-1,2,3,6-tetrahydropyridine mouse model of Parkinson's disease, *PLoS One* 4 (9) (2009), <https://doi.org/10.1371/journal.pone.0007247>.
- [37] K. Nishimaki, T. Asada, I. Ohsawa, E. Nakajima, C. Ikejima, T. Yokota, N. Kamimura, S. Ohta, Effects of molecular hydrogen assessed by an animal model and a randomized clinical study on mild cognitive impairment, *Curr. Alzheimer Res.* 15 (2018) 482–492, <https://doi.org/10.2174/1567205014666171106145017>.
- [38] I. Ohsawa, M. Ishikawa, K. Takahashi, M. Watanabe, K. Nishimaki, K. Yamagata, K.-I. Katsura, Y. Katayama, S. Aosh, S. Ohta, Hydrogen acts as a therapeutic antioxidant by selectively reducing cytotoxic oxygen radicals, *Nat. Med.* 13 (2007) 688–694, <https://doi.org/10.1038/nm1577>.
- [39] J. Kuhlmann, I. Bartsch, E. Willbold, S. Schuchardt, O. Holz, N. Hort, D. Höche, W.R. Heineman, F. Witte, Fast escape of hydrogen from gas cavities around corroding magnesium implants, *Acta Biomater.* 9 (2013) 8714–8721, <https://doi.org/10.1016/j.actbio.2012.10.008>.
- [40] T.M. Hopkins, K.J. Little, J.J. Vennemeyer, J.L. Triozzi, M.K. Turgeon, A.M. Heilman, D. Minter, K. Marra, D.B. Hom, S.K. Pixley, Short and long gap peripheral nerve repair with magnesium metal filaments, *J. Biomed. Mater. Res. Part A* 105 (2017) 3148–3158, <https://doi.org/10.1002/jbm.a.36176>.
- [41] J.J. Vennemeyer, T. Hopkins, M. Hershovitch, K.D. Little, M.C. Hagen, D. Minter, D.B. Hom, K. Marra, S.K. Pixley, Initial observations on using magnesium metal in peripheral nerve repair, *J. Biomater. Appl.* 29 (2015) 1145–1154, <https://doi.org/10.1177/0885328214553135>.
- [42] R.S. Bezawada, D.D. Jamiolkowski, I.-Y. Lee, V. Agarwal, J. Persival, S. Trenka-Benthin, M. Ermeta, J. Suryadevara, A. Yang, S. Liu, Monocryl® suture, a new ultra-pliable absorbable monofilament suture, *Biomaterials* 16 (1995) 1141–1148, [https://doi.org/10.1016/0142-9612\(95\)93577-Z](https://doi.org/10.1016/0142-9612(95)93577-Z).
- [43] P.D. Darney, S.E. Monroe, C.M. Klaisle, A. Alvarado, Clinical evaluation of the Capron contraceptive implant: preliminary report, *Am. J. Obstet. Gynecol.* 160 (1989) 1292–1295, [https://doi.org/10.1016/S0002-9378\(89\)80015-8](https://doi.org/10.1016/S0002-9378(89)80015-8).
- [44] M.A. Woodruff, D.W. Huttmacher, The return of a forgotten polymer – polycaprolactone in the 21st century, *Prog. Polym. Sci.* 35 (2010) 1217–1256, <https://doi.org/10.1016/j.progpolymsci.2010.04.002>.
- [45] A. Abdal-hay, N.A.M. Barakat, J.K. Lim, Influence of electrospinning and dip-coating techniques on the degradation and cytocompatibility of Mg-based alloy, *Colloids Surfaces A Physicochem. Eng. Asp.* 420 (2013) 37–45, <https://doi.org/10.1016/j.colsurfa.2012.12.009>.
- [46] J. Kim, H.M. Mousa, C.H. Park, C.S. Kim, Enhanced corrosion resistance and biocompatibility of AZ31 Mg alloy using PCL/ZnO NPs via electrospinning, *Appl. Surf. Sci.* 396 (2017) 249–258, <https://doi.org/10.1016/j.apsusc.2016.10.092>.
- [47] G.K. Soujanya, T. Hanas, V.Y. Chakrapani, B.R. Sunil, T.S.S. Kumar, Electrospun nanofibrous polymer coated magnesium alloy for biodegradable implant applications, *Int. Conf. Adv. Manuf. Mater. Eng. ICAMME 2014* (5) (2014) 817–823, <https://doi.org/10.1016/j.mspro.2014.07.333>.
- [48] S.C. Cifuentes, F. Bensiamar, A.M. Gallardo-Moreno, T.A. Osswald, J.L. González-Carrasco, R. Benavente, M.L. González-Martín, E. García-Rey, N. Vilaboa, L. Saldaña, Incorporation of Mg particles into PLLA regulates mesenchymal stem cell and macrophage responses, *J. Biomed. Mater. Res. – Part A* 104 (2016) 866–878, <https://doi.org/10.1002/jbm.a.35625>.
- [49] B. Li, H. Cao, Y. Zhao, M. Cheng, H. Qin, T. Cheng, Y. Hu, X. Zhang, X. Liu, In vitro and in vivo responses of macrophages to magnesium-doped titanium, *Sci. Rep.* 7 (2017), <https://doi.org/10.1038/srep42707>.
- [50] M.A.D. Boakye, N.P. Rijal, U. Adhikari, N. Bhattarai, Fabrication and characterization of electrospun PCL-MgO-keratin-based composite nanofibers for biomedical applications, *Materials* (Basel) 8 (2015) 4080–4095, <https://doi.org/10.3390/ma8074080>.
- [51] A. Edwards, D. Jarvis, T. Hopkins, S. Pixley, N. Bhattarai, Poly(ϵ -caprolactone)/keratin-based composite nanofibers for biomedical applications, *J. Biomed. Mater. Res. Part B Appl. Biomater.* 103 (2015) 21–30, <https://doi.org/10.1002/jbm.b.33172>.
- [52] E.J. Chong, T.T. Phan, I.J. Lim, Y.Z. Zhang, B.H. Bay, S. Ramakrishna, C.T. Lim, Evaluation of electrospun PCL/gelatin nanofibrous scaffold for wound healing and layered dermal reconstitution, *Acta Biomater.* 3 (2007) 321–330, <https://doi.org/10.1016/j.actbio.2007.01.002>.
- [53] M.F. Ryan, H. Barbour, Magnesium measurement in routine clinical practice, *Ann. Clin. Biochem.* 35 (1998) 449–459, <https://doi.org/10.1177/000456329803500401>.
- [54] J. O'Brien, I. Wilson, T. Orton, F. Pognan, Investigation of the Alamar Blue (resazurin) fluorescent dye for the assessment of mammalian cell cytotoxicity, *Eur. J. Biochem.* 267 (2000) 5421–5426, <https://doi.org/10.1046/j.1432-1327.2000.01606.x>.
- [55] T.M. Hopkins, A.M. Heilman, J.A. Liggett, K. LaSance, K.J. Little, D.B. Hom, D.M. Minter, K.G. Marra, S.K. Pixley, Combining micro-computed tomography with histology to analyze biomedical implants for peripheral nerve repair, *J. Neurosci. Methods* 255 (2015) 122–130, <https://doi.org/10.1016/j.jneumeth.2015.08.016>.
- [56] K.-J. Jeon, H.R. Moon, A.M. Ruminski, B. Jiang, C. Kisielowski, R. Bardhan, J.J. Urban, Air-stable magnesium nanocomposites provide rapid and high-capacity hydrogen storage without using heavy-metal catalysts, *Nat. Mater.* 10 (2011) 286–290, <https://doi.org/10.1038/nmat2978>.
- [57] E.M. Abdelrazek, A.M. Hezma, A. El-khodary, A.M. Elzayat, Spectroscopic studies and thermal properties of PCL/PMMA biopolymer blend, *Egypt. J. Basic Appl. Sci.* 3 (2016) 10–15, <https://doi.org/10.1016/j.ejbas.2015.06.001>.
- [58] J.M. Adams, Particle size and shape effects in materials science: examples from polymer and paper systems, *Clay Miner.* 28 (1993) 509–530, <https://doi.org/10.1180/claymin.1993.028.4.03>.
- [59] A.J. Kinloch, D.L. Maxwell, R.J. Young, The fracture of hybrid-particulate composites, *J. Mater. Sci.* 20 (1985) 4169–4184, <https://doi.org/10.1007/BF00552413>.
- [60] R. Petrucci, L. Torre, 2 – Filled Polymer Composites, in: C.F. Jasso-Gastinel, J.M. Kenny (Eds.), *Modif. Polym. Prop.*, William Andrew Publishing, 2017: pp. 23–46, <https://doi.org/10.1016/B978-0-323-44353-1.00002-6>.
- [61] D.L. Heath, R. Vink, Optimization of magnesium therapy after severe diffuse axonal brain injury in rats, *J. Pharmacol. Exp. Ther.* 288 (1999) 1311–1316, ISSN: 00223565.
- [62] J. Wang, F. Witte, T. Xi, Y. Zheng, K. Yang, Y. Yang, D. Zhao, J. Meng, Y. Li, W. Li, K. Chan, L. Qin, Recommendation for modifying current cytotoxicity testing standards for biodegradable magnesium-based materials, *Acta Biomater.* 21 (2015) 237–249, <https://doi.org/10.1016/j.actbio.2015.04.011>.
- [63] E. Martín-López, M. Nieto-Díaz, M. Nieto-Sampedro, Differential adhesiveness and neurite-promoting activity for neural cells of chitosan, gelatin, and poly-L-lysine films, *J. Biomater. Appl.* 26 (2012) 791–809, <https://doi.org/10.1177/0885328210379928>.
- [64] J.J. Vennemeyer, T. Hopkins, J. Kuhlmann, W.R. Heineman, S.K. Pixley, Effects of elevated magnesium and substrate on neuronal numbers and neurite outgrowth of neural stem/progenitor cells in vitro, *Neurosci. Res.* 84 (2014) 72–78, <https://doi.org/10.1016/j.neures.2014.05.001>.
- [65] J.M. Anderson, S. Jiang, Implications of the acute and chronic inflammatory response and the foreign body reaction to the immune response of implanted biomaterials, in: *Immune Response to Implant. Mater. Devices Impact Immune Syst. Success an Implant*, Springer International Publishing, 2016, pp. 15–36, doi: 10.1007/978-3-319-45433-7_2.
- [66] M.E. Scarritt, R. Londono, S.F. Badylak, Host response to implanted materials and devices: an overview, in: *Immune Response to Implant. Mater. Devices Impact Immune Syst. Success an Implant*, Springer International Publishing, 2016, pp. 1–14, doi: 10.1007/978-3-319-45433-7_1.
- [67] R.B. Caldwell, H.A. Toque, S.P. Narayanan, R.W. Caldwell, Arginase: an old enzyme with new tricks, *Trends Pharmacol. Sci.* 36 (2015) 395–405, <https://doi.org/10.1016/j.tips.2015.03.006>.
- [68] L. Campbell, C.R. Saville, P.J. Murray, S.M. Cruickshank, M.J. Hardman, Local arginase 1 activity is required for cutaneous wound healing, *J. Invest. Dermatol.* 133 (2013) 2461–2470, <https://doi.org/10.1038/jid.2013.164>.
- [69] D. Hachim, S.T. LoPresti, C.C. Yates, B.N. Brown, Shifts in macrophage phenotype at the biomaterial interface via IL-4 eluting coatings are associated with improved implant integration, *Biomaterials* 112 (2017) 95–107, <https://doi.org/10.1016/j.biomaterials.2016.10.019>.
- [70] S.-C. Wong, A. Baji, S. Leng, Effect of fiber diameter on tensile properties of electrospun poly(ϵ -caprolactone), *Polymer* (Guildf.) 49 (2008) 4713–4722, <https://doi.org/10.1016/j.polymer.2008.08.022>.
- [71] H. Sun, L. Mei, C. Song, X. Cui, P. Wang, The in vivo degradation, absorption and excretion of PCL-based implant, *Biomaterials* 27 (2006) 1735–1740, <https://doi.org/10.1016/j.biomaterials.2005.09.019>.
- [72] T. Finkel, N.J. Holbrook, Oxidants, oxidative stress and the biology of ageing, *Nature* 408 (2000) 239–247, <https://doi.org/10.1038/35041687>.
- [73] S.M. Ostojic, M.D. Stojanovic, Hydrogen-rich water affected blood alkalinity in physically active men, *Res. Sport. Med.* 22 (2014) 49–60, <https://doi.org/10.1080/15438627.2013.852092>.

- [74] F. Feyerabend, F. Witte, M. Kammal, R. Willumeit, Unphysiologically high magnesium concentrations support chondrocyte proliferation and redifferentiation, *Tissue Eng.* 12 (2006) 3545–3556, <https://doi.org/10.1089/ten.2006.12.3545>.
- [75] S. Mostofi, E.B. Rad, H. Wiltsche, U. Fasching, G. Szakacs, C. Ramskogler, S. Srinivasaiah, M. Ueçal, R. Willumeit, A.-M. Weinberg, U. Schaefer, Effects of corroded and non-corroded biodegradable mg and mg alloys on viability, morphology and differentiation of MC3T3-E1 cells elicited by direct cell/material interaction, *PLoS One* 11 (2016), <https://doi.org/10.1371/journal.pone.0159879>.
- [76] H.M. Wong, S. Wu, P.K. Chu, S.H. Cheng, K.D.K. Luk, K.M.C. Cheung, K.W.K. Yeung, Low-modulus Mg/PCL hybrid bone substitute for osteoporotic fracture fixation, *Biomaterials* 34 (2013) 7016–7032, <https://doi.org/10.1016/j.biomaterials.2013.05.062>.
- [77] T. Yu, V.J. Tutwiler, K. Spiller, The role of macrophages in the foreign body response to implanted biomaterials, in: *Biomater. Regen. Med. Immune Syst.*, Springer International Publishing, 2015, pp. 17–34. doi: 10.1007/978-3-319-18045-8_2.
- [78] J. Kzhyshkowska, A. Gudima, V. Riabov, C. Dollinger, P. Lavalle, N.E. Vrana, Macrophage responses to implants: prospects for personalized medicine, *J. Leukoc. Biol.* 98 (2015) 953–962, <https://doi.org/10.1189/jlb.5VMR0415-166R>.
- [79] R. Sridharan, A.R. Cameron, D.J. Kelly, C.J. Kearney, F.J. O'Brien, Biomaterial based modulation of macrophage polarization: a review and suggested design principles, *Mater. Today* 18 (2015) 313–325, <https://doi.org/10.1016/j.mattod.2015.01.019>.
- [80] A. Das, M. Sinha, S. Datta, M. Abas, S. Chaffee, C.K. Sen, S. Roy, Monocyte and macrophage plasticity in tissue repair and regeneration, *Am. J. Pathol.* 185 (2015) 2596–2606, <https://doi.org/10.1016/j.ajpath.2015.06.001>.
- [81] S. Galván-Peña, L.A.J. O'Neill, Metabolic reprogramming in macrophage polarization, *Front. Immunol.* 5 (2014), <https://doi.org/10.3389/fimmu.2014.00420>.
- [82] J.T. Pesce, T.R. Ramalingam, M.M. Mentink-Kane, M.S. Wilson, K.C.E. Kasmi, A. M. Smith, R.W. Thompson, A.W. Cheever, P.J. Murray, T.A. Wynn, Arginase-1-expressing macrophages suppress Th2 cytokine-driven inflammation and fibrosis, *PLoS Pathog.* 5 (2009), <https://doi.org/10.1371/journal.ppat.1000371>.
- [83] A. Brown, S. Zaky, H. Ray Jr., C. Sfeir, Porous magnesium/PLGA composite scaffolds for enhanced bone regeneration following tooth extraction, *Acta Biomater.* 11 (2015) 543–553, <https://doi.org/10.1016/j.actbio.2014.09.008>.
- [84] N. Mokarram, R.V. Bellamkonda, A perspective on immunomodulation and tissue repair, *Ann. Biomed. Eng.* 42 (2014) 338–351, <https://doi.org/10.1007/s10439-013-0941-0>.
- [85] A.D. Joshi, S.R. Oak, A.J. Hartigan, W.G. Finn, S.L. Kunkel, K.E. Duffy, A. Das, C.M. Hogaboam, Interleukin-33 contributes to both M1 and M2 chemokine marker expression in human macrophages, *BMC Immunol.* 11 (2010), <https://doi.org/10.1186/1471-2172-11-52>.
- [86] Y. Tatano, T. Shimizu, H. Tomioka, Unique macrophages different from M1/M2 macrophages inhibit T cell mitogenesis while upregulating Th17 polarization, *Sci. Rep.* 4 (2014), <https://doi.org/10.1038/srep04146>.
- [87] Z. Cao, R.J. Gilbert, W. He, Simple agarose-chitosan gel composite system for enhanced neuronal growth in three dimensions, *Biomacromolecules* 10 (2009) 2954–2959, <https://doi.org/10.1021/bm900670n>.
- [88] E. Saino, M.L. Focarete, C. Gualandi, E. Emanuele, A.I. Cornaglia, M. Imbriani, L. Visai, Effect of electrospun fiber diameter and alignment on macrophage activation and secretion of proinflammatory cytokines and chemokines, *Biomacromolecules* 12 (2011) 1900–1911, <https://doi.org/10.1021/bm200248h>.
- [89] A.K. Blakney, M.D. Swartzlander, S.J. Bryant, The effects of substrate stiffness on the in vitro activation of macrophages and in vivo host response to poly (ethylene glycol)-based hydrogels, *J. Biomed. Mater. Res. A* 100 (2012) 1375–1386, <https://doi.org/10.1002/jbm.a.34104> [doi].
- [90] M. Friedemann, L. Kalbitzer, S. Franz, S. Moeller, M. Schnabelrauch, J.-C. Simon, T. Pompe, K. Franke, Instructing human macrophage polarization by stiffness and glycosaminoglycan functionalization in 3D collagen networks, *Adv. Healthc. Mater.* 6 (2017), <https://doi.org/10.1002/adhm.201600967>.
- [91] H. Lv, H. Wang, Z. Zhang, W. Yang, W. Liu, Y. Li, L. Li, Biomaterial stiffness determines stem cell fate, *Life Sci.* 178 (2017) 42–48, <https://doi.org/10.1016/j.lfs.2017.04.014>.
- [92] S. Chen, J.A. Jones, Y. Xu, H.-Y. Low, J.M. Anderson, K.W. Leong, Characterization of topographical effects on macrophage behavior in a foreign body response model, *Biomaterials* 31 (2010) 3479–3491, <https://doi.org/10.1016/j.biomaterials.2010.01.074>.
- [93] K. Garg, N.A. Pullen, C.A. Oskeritzian, J.J. Ryan, G.L. Bowlin, Macrophage functional polarization (M1/M2) in response to varying fiber and pore dimensions of electrospun scaffolds, *Biomaterials* 34 (2013) 4439–4451, <https://doi.org/10.1016/j.biomaterials.2013.02.065>.
- [94] E.M. Sussman, M.C. Halpin, J. Muster, R.T. Moon, B.D. Ratner, Porous implants modulate healing and induce shifts in local macrophage polarization in the foreign body reaction, *Ann. Biomed. Eng.* 42 (2014) 1508–1516, <https://doi.org/10.1007/s10439-013-0933-0>.
- [95] J.E. Sanders, S.D. Bale, T. Neumann, Tissue response to microfibers of different polymers: polyester, polyethylene, polylactic acid, and polyurethane, *J. Biomed. Mater. Res.* 62 (2002) 222–227, <https://doi.org/10.1002/jbm.10285>.
- [96] F. Alvarez, R.M. Lozano Puerto, B. Pérez-Maceda, C.A. Grillo, M. Fernández Lorenzo De Mele, Time-lapse evaluation of interactions between biodegradable Mg particles and cells, *Microsc. Microanal.* 22 (2016) 1–12, <https://doi.org/10.1017/S1431927615015597>.
- [97] L. Mao, L. Shen, J. Chen, X. Zhang, M. Kwak, Y. Wu, R. Fan, L. Zhang, J. Pei, G. Yuan, C. Song, J. Ge, W. Ding, A promising biodegradable magnesium alloy suitable for clinical vascular stent application, *Sci. Rep.* 7 (2017), <https://doi.org/10.1038/srep46343>.